Research Square

Preprints are preliminary reports that have not undergone peer review.
They should not be considered conclusive, used to inform clinical practice,
or referenced by the media as validated information.

Sequential acid–alkali treatment for the identification and removal of fluoride-bearing zeolitic species from agricultural soil

Mamata Bhoi
Maa Manikeshwari University
Trilochan Swain
scienceorissa@gmail.com
Fakir Mohan University

Research Article

Keywords: Fluoride, Agricultural soil, Fluoride leaching, Zeolitic compounds, ISE

Posted Date: November 13th, 2026

DOI: https://doi.org/10.21203/rs.3.rs-11405074/v1

License: This work is licensed under a Creative Commons Attribution 4.0 International License.
Read Full License

Additional Declarations: No competing interests reported.

Sequential acid–alkali treatment for the identification and removal of fluoride-bearing zeolitic species from agricultural soil

Mamata Bhoi[1] and Trilochan Swain[2*]

1. Assistant Professor, Department of Chemistry, Maa Manikeshwari University, Bhawanipatna-766001, Kalahandi, Odisha, India.
2. Associate Professor, P.G. Department of Chemistry, Fakir Mohan University, Nuapadhi, Balasore-756089, Odisha, India

*Corresponding address

E-mail: scienceorissa@gmail.com (Trilochan swain)

ORCID: http://orcid.org/ 0000-0002-1617-8351

Abstract

Fluorosis results from excessive fluoride intake, mainly via drinking water and food. To prevent this, it is crucial to identify and eliminate fluoride sources in agricultural soils, ensuring fluoride levels stay below the WHO guideline of 1.5 mg L^{-1}. This study involved collecting and analysing surface soil samples to determine the origin and chemical forms of fluoride entering the food chain. The soils underwent sequential acid and alkali treatments to extract fluoride compounds, with fluoride levels measured at various pH values using a fluoride ion-selective electrode (ISE). The highest fluoride concentration (296 mg L^{-1}) was detected in the acid leachate at pH 11.17. After alkali treatment, fluoride levels dropped to 1.22 mg L^{-1} at pH 11.03 and below detection ($<10^{-4}$ mg L^{-1}) at pH 8.59. Solid-state ^{27}Al NMR spectroscopy of the acid-treated soil showed the disappearance of the resonance around 165 ppm, indicating complete removal of fluoride-containing aluminium species. Additionally, alkali treatment neutralised fluoride associated with zeolitic phases, confirmed by a turbidity test with $Ca(OH)_2$. These findings suggest that sequential acid–alkali treatment effectively removes fluoride-bearing zeolitic species, $[AHFS - HZSM - 5]xF_2$ from soils, offering a practical approach to reduce fluoride transfer into the food chain.

Keywords: Fluoride, Agricultural soil, Fluoride leaching, Zeolitic compounds, ISE

1 Introduction

Fluoride is the 13th most abundant element in Earth's crust and is essential for humans and animals in trace amounts in drinking water (0.7 mg L^{-1}) over the temperature range 298 K to

303 K [**1**]. Fluoride reduces tooth decay by 40% during dental enamel development [**2**]. At 281-285 K, fluoride concentration in safe drinking water can reach 1.5 mg L^{-1}, per WHO standards. Fluoride, the most electronegative element, is present in soil, rock, water, plants, and animals, including humans [**3**]. There are two sources of fluoride contamination in the earth: natural and anthropogenic, with the latter arising from processes such as rock leaching and the use of fertilisers and pesticides [**4**]. One of the processes is anthropogenic, due to human activities in industry, the use of fluoride-containing pesticides, and motorisation, which pollute the environment, including air, water, and soil, with fluoridation [**5**]. Fluoride enters the animal food chain through drinking water, as it is present in air, water, and food. Fluoride-containing drinking water causes endemic fluorosis, which is found in at least 25 countries worldwide. It is primarily found in India, China, and parts of Africa. Other diseases, such as crippling bone deformities, intellectual decline, reduced cognitive ability, and impaired growth, have been reported with long-term use of fluoride-containing drinking water, but no clear link to bone cancer [**6-10**]. Among the various sources of fluoride reserves, rocks and minerals have the highest fluoride content. The average fluoride concentration in rock minerals is 625 mg L^{-1}. In India, rocks in Coimbatore district, Tamil Nadu, contain 180-2600 mg L^{-1} fluoride [**11**]. The highest fluoride concentration minerals are syenites (Na_2O & K_2O with 2-10% F), granites, monzonites, quartz (CaF_2 & SiO_2), felsic rocks, biotite [$K(Mg, Fe)_3AlSi_3O_{10}(F, OH)_2$], and alkaline volcanics [**12-13**]. The most abundant fluoride-rich minerals in rocks and sediments include fluorite (CaF_2), fluoroapatite [$Ca_5(PO_4)_3F$], micas, and topaz [$Al_2(SiO_4)F_2$], etc. [**14-15**]. Fluoride contamination in soil and water mainly results from acidic volcanic rocks, basic dikes, granites, and hornblende [**16**]. The fluoride in groundwater is believed to result from interactions with the wall rock [**15, 17**]. Fluoride is mainly released from the hydroxy positions of hornblende silicate minerals and is further concentrated by evapotranspiration. After concentration, the soil and groundwater exhibit residual alkalinity. Water flows from the tops of the hills to the valley bottoms, precipitating calcite, dolomite, and fluorite [**11**]. The fluoride content in most rocks and soils ranges from 100 to 1300 mg L^{-1} and from 20 to 500 mg L^{-1}, respectively [**18-19**]. According to WHO standards, fluoride concentration in soil ranges from 200 mg L^{-1} to 300 mg L^{-1}, but fluoride release from soil is difficult to predict because factors such as climate, soil chemistry, and chemical speciation influence it [**20**]. The slow release of fluoride from the soil is due to the presence of clay and phosphorite [**21**]. Aluminium leaching from soil increases in the presence of high fluoride concentrations [**22-23**]. There are other sources of fluoride contamination in soil and groundwater, such as volcanic ash, wet and dry gas deposition, and the use of phosphate fertilisers, fumigants, insecticides, etc. The ash from

the Hekla eruption contains 23-35 mg L^{-1} fluoride. The risk of fluoride contamination increases due to the high solubility of volcanic ash [**24**]. There are various anthropogenic processes, such as aluminum smelters, iron and steel manufacture, ceramic industries, use of fertilisers, fossil fuel burning, etc., that are responsible for fluoride contamination due to the release of fluoride-containing fumes like HF, SiF_4, F_2, and particulate materials like CaF_2, NaF, and Na_2SiF_6, which are further soluble and precipitate in the ground [**25-27**]. In China, fluoride contamination results from two factors: first, interactions between the recharge area and fluoride-containing minerals in rocks. Second, evaporation and mixing of karst water lead to high fluoride contamination [**28**]. In South Korea, fluoride contamination is due to residence time, as the fluoride source is geogenic [**29**]. In Japan, fluoride contamination is due to volcanic ash, which contains 788.1 mg L^{-1}. Ash is highly soluble. Fluoride oversaturation is another cause of fluoride contamination. This oversaturation results from weathering and the alteration of granitic rocks [**17, 30**]. In Pakistan, fluoride contamination is due to several factors, such as the use of fertiliser, which contains 53-255 mg L^{-1}; the use of coal that contains 5-20 mg L^{-1}; granite rocks contain an average fluoride of 1939 mg L^{-1}, and primary and secondary kaolin contain 468-1722 mg L^{-1} and 270 mg L^{-1}, respectively. Fluoride contamination in groundwater affects more than 2 million people [**31**]. In Sri Lanka, fluoride contamination has persisted for more than two decades in the low plains due to longer residence times with geological minerals and slower groundwater movement than in the highlands [**32**]. In Turkey, fluoride contamination results from leaching from volcanic rocks and the Gölcük pyroclastic and Miocene clastic rocks, which contain about 0.39-5.62 mg L^{-1} [**33**]. In Iran, soil and groundwater are contaminated by excessive use of chemical fertilisers (nitrogen and phosphate) and by excessive groundwater extraction for agricultural processes [**34**]. In Greece and Poland, soil is contaminated with fluoride due to alumina [**35**] and the phosphate industry. In Poland, fluoride is naturally present in aquifers at about 7 mg L^{-1} [**36**]. In Africa, volcanic activity leads to high fluoride contamination in Tanzania, with fluoride concentrations of about 1640-2800 mg L^{-1} in the lakes of the East African Rift [**37**]. Fluoride contamination of natural waters in Kenya is due to evaporation [**24**]. In the USA, fluoride contamination comes from both industrial and natural processes. Fluoride in deep aquifers in the Western US is 5-15 mg L^{-1}. In Southern California, the fluoride in the Lakeland ranges from 3.6 to 5.3 mg L^{-1}. In addition to the above fluoride-contaminated areas, other parts of the USA, such as Iowa, Kansas, Nevada, and North Carolina, are also contaminated with fluoride [**38**]. Fluoride contamination in the US and Canada is mainly due to industrial processes.

In India, groundwater fluoride content increases due to evapotranspiration, which increases residual alkalinity. Some aquifers in Maharashtra were also contaminated with fluoride due to prolonged residence time [**39-40**]. Almost all rocks in southern India are rich in fluoride minerals, which is why soil and groundwater are contaminated with fluoride. The fluoride content in the granites of Nalgonda and Hyderabad in Andhra Pradesh is 325-3200 mg L^{-1} and 910 mg L^{-1}, respectively [**41**]. In Balasore, Odisha, India, groundwater and soil are highly contaminated with fluoride. Fluorosis also affects parts of the Balasore district, as in other parts of India [**42**] and in countries like China [**43**], Iran [**44**], and Turkey [**45**]. The thermal and spectroscopic study of the fluoride-contaminated soil dug 40 ft below ground level indicates that the contamination is due to the presence of fluoride minerals of aluminium, silicon, and iron [**46**]. The main purpose of the spectroscopic and thermal study of the surface soil (20 cm depth from ground level) contaminated with fluoride is to investigate the role of fluoride minerals in contaminating the surface soil, which affects the food produced by plants, as described elsewhere [**34**]. The examined soil is covered with a mini forest, where the plants' leaves are left to decompose naturally, whereas the published soil was collected from 40ft below the surface of the bare land, where groundwater is primarily extracted for drinking. Both soils were collected from the Fakir Mohan University campus. Quantitative measurement of fluoride in the surface soil was carried out on the solution after leaching the soil with conc. HNO_3 at different acidities.

2 Materials and Methods

2.1 Soil collection

The soil was collected from 7 sample sites of 20×20 m^2 land using a screw auger at a depth of 20 cm below ground level, at a DMS latitude of 21° 32' 47.4972" N and a DMS Longitude of 86° 48' 58.2912" E. All the soil samples were mixed, air-dried in the shed, and ground in a wooden roller. The air-dried sample was sieved through a 2 mm stainless steel sieve. This sieved soil sample was stored in a polythene jar.

2.2 Sample preparation

The collected, air-dried, and sieved soil is called the original soil. The original soil was treated with Conc. HNO_3 for acid leaching and Conc. NH_3 for alkaline leaching. The use of Conc. HNO_3 for leaching fluoride from the soil is described elsewhere [**47**]. HCl is known to be better for leaching fluoride from soil. We use conc. HNO_3 for possible removal of fluoride from silicate-related minerals after keeping for 10 days. The use of Conc. HNO_3 was purchased from Merck (CAS number 7697-37-2). The original soil (10 g) was treated with 5 M conc. HNO_3

with constant stirring for up to 5 h. This acid-treated original soil was kept for 10 days with occasional stirring. The original soil treated with Conc. HNO_3 was filtered. The soil residue was called acid-treated soil, and the filtrate (called acid filtrate) was retained for quantitative fluoride measurement at different acidity levels using an ISE. The pH of the acid filtrate was adjusted using a $Ca(OH)_2$, turbidity solution. The acid-treated soil was collected after several washings with distilled water and used for various spectroscopic measurements (IR, NMR, DRS), thermal behaviour (TG-DTA, specific heat capacity), and SEM imaging for morphological analysis.

The alkaline fertiliser is basically used in farmland for vegetable cultivation. To determine its effect in fluoride-contaminated soil, alkaline leaching of soil was carried out. Alkaline leaching of soil is described elsewhere [**48**]. For alkaline leaching, Conc. NH_3 was purchased from Merck (CAS number 1336-21-6). 10 g of the original soil was treated with Conc. NH_3, and the mixture was stirred for about 5 h to ensure homogeneity. This solution was kept for 10 days with occasional stirring. This original soil solution was filtered, and the residue was called alkali-treated soil. The filtrate (alkaline filtrate) was retained for further analysis. The alkali-treated soil was washed with distilled water and collected for the different measurements described for the acid-leached soil. Both acid- and alkali-treated soils are called chemically treated soils. All the above measurements were also conducted on the original soil.

2.3 Instrumentation

All ^{19}F, ^{27}Al, and ^{29}Si NMR spectra were acquired at room temperature in the solid state for both the original and chemically treated soils. All these NMR measurements were acquired at SAIF, IISc, Bangalore, using a single-pulse 400 MHz JEOL ECX400 spectrometer. The FTIR was measured in the solid state using a Bruker Alpha Platinum with a spectral range of 450-4000 cm^{-1}. The Diffuse Reflectance Spectra (DRS) were acquired in the solid state using a Perkin-Elmer Lambda 950 UV-Vis-NIR spectrophotometer over the spectral range of 200 nm to 1100 nm. The LECO TruSpec Micro analyser was used to determine the C, H, and N content of the original soil. Thermogravimetric Differential Scanning Calorimetry (TG-DSC) was used to determine the soil's moisture and heat capacity. This was measured using a Netzsch STA 449 F3 Jupiter over the temperature range 298 K to 1068 K in an N_2 atmosphere at a heating rate of 10 K min^{-1}. This measurement was acquired using an Al_2O_3 (Alumina) crucible. The specific heat capacity (C_P) was measured in an N_2 atmosphere at a heating rate of 2K min^{-1} over the temperature range 268 K to 358 K. The C_P was measured using a NETZSCH DSC 204F1 Phoenix with a Concavus Al, pierced lid. SEM with EDAX was performed on a JEOL 6390LA/OXFORD XMX N with a Tungsten filament at SAIF, Kochi, to study the

morphology. Fluoride in the acid leachate (acid filtrate) was measured using an ISE on the HANNA HI 98402 fluoride meter. The fluoride meter was calibrated with a buffer before measurement. The pH of the acid-leaching solution (acid filtrate) was measured using a buffer-calibrated Systronics Digital pH meter. The FTIR, TG-DSC, UV-Vis-NIR (DRS), Specific heat capacity, and elemental analysis were measured at SAIF, IIT Madras.

3 Results

3.1 Reflectance spectrum

3.1.1 Original soil

The DRS of soil in the range 200 nm to 1100 nm is shown in Supplementary **Fig.S1a**. The average reflectance of this soil is approximately 7% in the low-wavelength region (i.e., up to 500 nm). In contrast, the average reflectance of this soil is about 38% in the high-wavelength region i.e., up to 700 nm. The maximum reflectance is 45% at 700 nm. Soil with a moisture content of 0.32 g cm^{-3} shows 15% reflectance, while soil with a moisture content of 0.07 g cm^{-3} shows less than 20%. Similarly, soil with a moisture content of 0.58 g cm^{-3} shows reflectance below 25%. All these reflectance measurements are in the visible region. This indicates that in low-moisture-content soil (< 0.32 g cm^{-3}), % reflectance decreases as soil moisture increases. In high-moisture-content soil (> 0.45 g cm^{-3}), % reflectance increases with increasing soil moisture. This soil is primarily composed of clay and sand. The proportions of clay and sand are ~25 % each [**49**]. Neema et al. studied the reflectance percentage at various soil moisture levels. They also found that reflectance decreases at a certain soil moisture level and then increases as soil moisture increases [**50**]. Soil collected from Clearwell Caves containing 70± 4% haematite has a reflectance of less than 30%. In contrast, soil collected from Clearwell Caves containing 70 ± 5% goethite shows a reflectance of 45% at wavelengths greater than 550 nm. Both soils have reflectance below 15% at wavelengths below 550 nm [**51**].

The soil's optical band gap, E_g, is calculated using DRS. This calculation uses the well-known Kubelka–Munk relation.

$$[F(R_\infty)hf]^{\frac{1}{\gamma}} = A(hf - E_g) \qquad (1)$$

The term γ value in equation (1) is either 0.5 or 2. This value depends upon the nature of the electronic transition between the bands. The γ = 0.5 is due to direct transition, and 2 is due to an indirect transition. The soil is classified as an insulator based on its band gap, E_g = 4.388 eV. This band gap is similar to that of soil containing fluoride minerals of silicon, aluminum, and iron [**46**].

This soil's refractive index (n_o) can be calculated using Moss and Ravindra's relation. Both these well-known relations are associated with the optical band gap (E_g). The Moss relation for calculating the refractive index (n_o) is given below.

$$n_o^4 E_g = 95\ eV \qquad (2)$$

The refractive index (n_o) of this soil is 2.16. This relation is also not strictly valid for high-energy optical band gaps. Due to the high optical band gap, E_g= 4.388 eV, the well-known Ravindra relation cannot be used for this soil type. This relation does not fit well for high optical band gaps (Eg > 4 eV) [**52**]. For high-energy band gaps, the Herve et al. relation is used to calculate the refractive index [**53**].

$$n_o = \sqrt{1 + \{13.6/(E_g + 3.4)\}^2} \qquad (3)$$

The calculated refractive index (n_o) using the above Herve et al. relation is 2.01. According to Moss and Herve et al., the refractive index of this soil is ~ 2.0. This refractive index (n_o) value of the examined soil signifies that light travels ~ 2.0 times slower than the speed of light in air. The dielectric constant (κ) is related to the permittivity (ε) of any material as follows.

$$\kappa = \frac{\varepsilon}{\varepsilon_o} \qquad (4)$$

Where, ε_o is the permittivity in free space, the dielectric constant (κ), and the refractive index (n_o) for a non-magnetised material, related as follows

$$n_o = \sqrt{\frac{\varepsilon}{\varepsilon_o}} = \sqrt{\kappa} \quad ; \qquad \kappa = n_o^2 \qquad (5)$$

The dielectric constant (κ) of this soil is calculated using the refractive index (n_o) value of Herve et al. and found to be 4.04.

3.1.2 Acid-treated soil

The DRS of the acid-treated soil in the range 200 nm to 2500 nm is displayed in Supplementary **Fig.S1b**. The % of average reflectance of this acid-treated soil is approximately 13 in the low-wavelength region, i.e., up to 500 nm from 200 nm. In contrast, the average reflectance of this soil is almost the same as that of the original soil, i.e., 38% in the high-wavelength region, up to 700 nm. The maximum reflectance is 46% at 700 nm. The refractive index calculated from the Moss relation is n_{ac} = 2.41.

3.1.3 Alkali-treated soil

The DRS of the alkali-treated soil in the range 200 nm to 2500 nm is displayed in Supplementary **Fig.S1c**. The % reflectance of this alkali-treated soil is approximately 13 in the

low-wavelength region, i.e., up to 500 nm from 200 nm. In contrast, the average reflectance of this soil is almost the same as that of the original soil, i.e., 36% in the high-wavelength region, up to 700 nm. This average reflectance is less than 2% for acid-treated and untreated soil. The maximum reflectance is 44% at 700 nm. The refractive index calculated from the Moss relation is $n_{al} = 2.43$.

3.1.4 Comparative DRS

Fig.1a displays the comparative DRS of acid-treated, alkali-treated, and the original soil in the range 200 nm to 1100 nm.

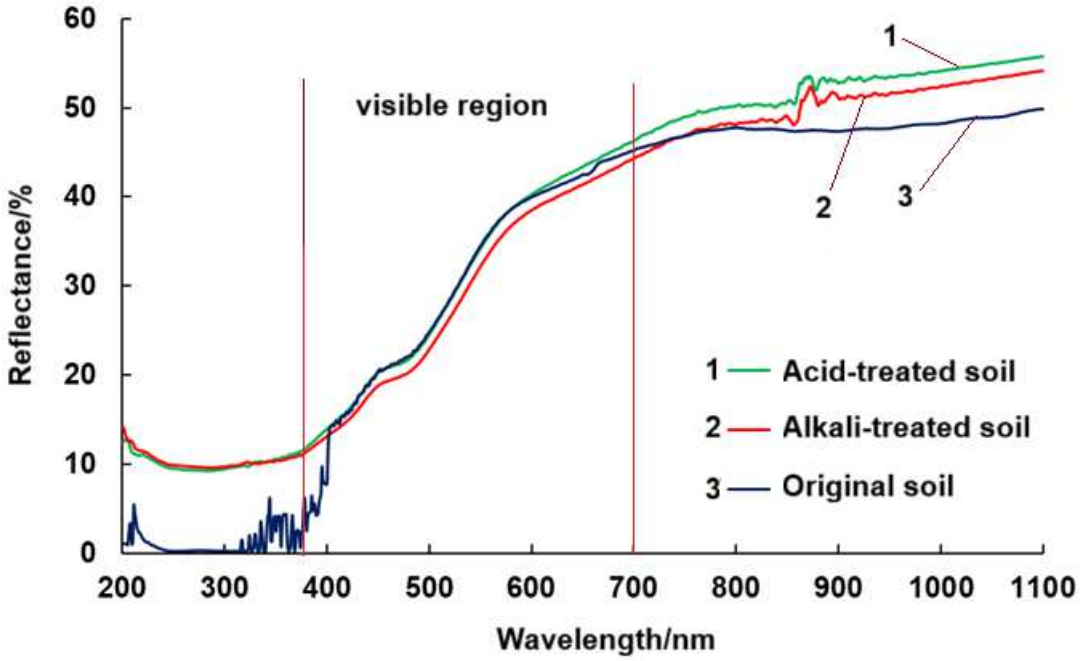


Fig.1a Comparative DRS of original, acid- and alkali-treated soil

The % reflectance of the acid- and alkali-treated soil is approximately similar to the soil containing 0.32 g cm^{-3} moisture, which shows 15 % reflectance in low-wavelength regions, i.e., up to 550 nm. This % reflectance is similar to that of the soil of Clearwell Caves, which contains 70± 4% and 70± 5% haematite in the low-wavelength regions, i.e., up to 550 nm [**49**, **51**]. The soil reflectance in bunded and non-bunded plots is ~5% at 500 nm and ~25% at 700 nm. The soil was collected from Aba Gerima, Ethiopia, a tropical highland. The major components % of the soil are sand (27.6±1.97), silt (28.2±1.03), clay (44.3±2.56), and organic carbon (1.65±0.13). The % reflectance of our soil is consistent with that of soil [**54**]. The comparative band gap (E_g) of the acid-treated, alkali-treated, and untreated soil is displayed in **Fig.1b**.

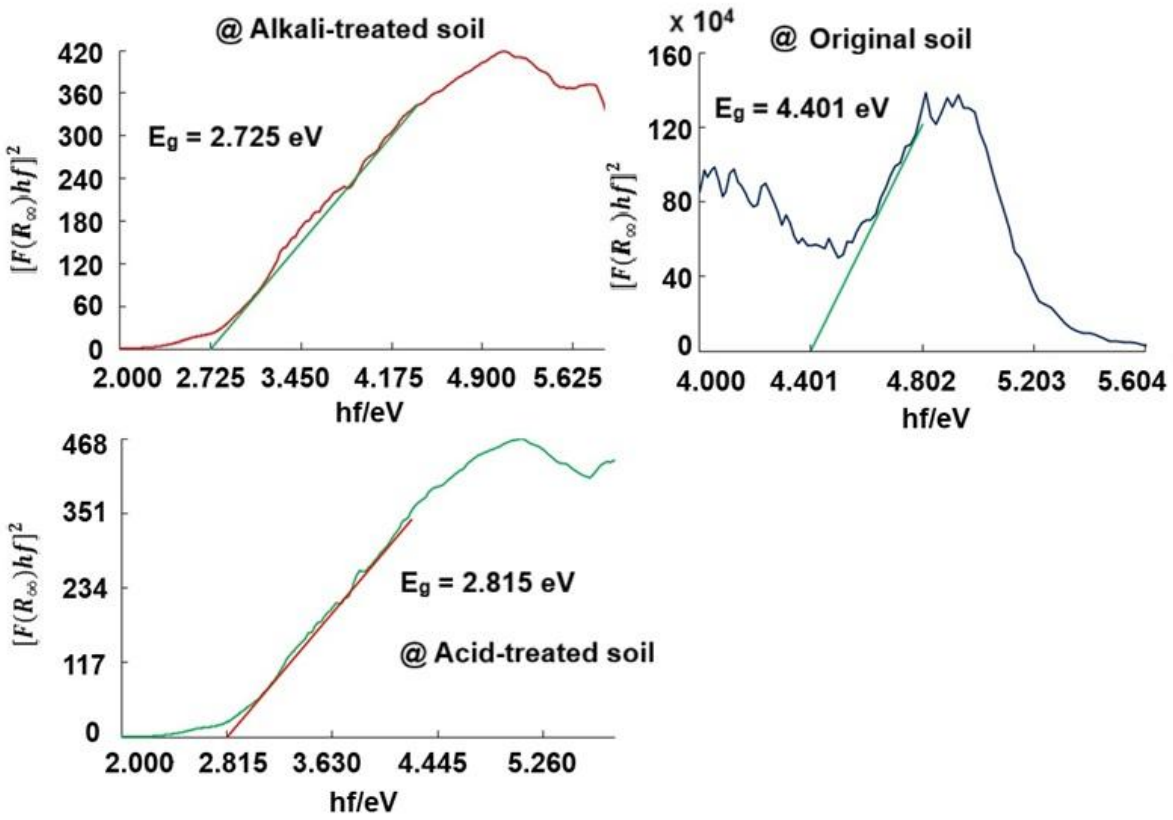


Fig.1b Comparative band gap of original, acid- and alkali-treated soil

The bandgap of the chemically treated soil is 2.725 eV, and 2.815 eV for the alkali- and acid-treated soil, respectively. The bandgap of the fayalite composite prepared from iron sand and laterite soil using reactive reagents is 2.75 eV, determined from a Tauc plot. DFT calculations using the plane-wave method compute the bandgap of this composite to be 2.88 eV, supported by Quantum Espresso [**55-56**]. Fayalite is an iron-rich silicate mineral. This indicates that the chemically treated soil is mineral-rich and contains silicates. NMR analysis of the chemically treated soil confirms this. The refractive index is inversely related to the material's porosity [**57**]. The chemically treated soil has a higher refractive index than the original soil. The refractive indices are in this order: $n_o < n_{ac} < n_{al}$. This indicates that chemical treatment decreases the soil's porosity.

3.2 FT-IR analysis

3.2.1 Original soil

The FTIR spectrum of this soil in the range 500 cm^{-1} to 4000 cm^{-1} is displayed in **Fig.2**.

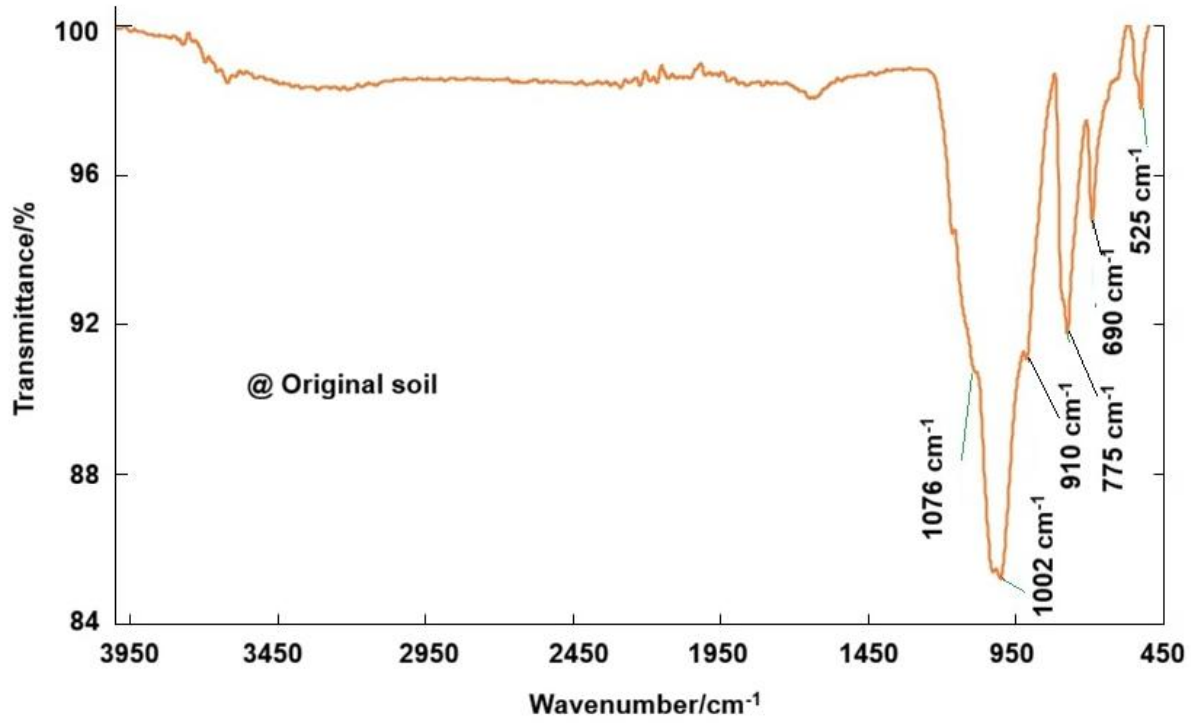


Fig. 2 FTIR spectrum of the original soil

The peak at 690 cm^{-1} is assigned to the Al-F stretching mode, rather than the 700 cm^{-1} stretching mode reported in the literature [**58**]. This indicates that this fluorine-contaminated soil contains either AlF_3 or AlO_xF_y. Upon fluorine exposure, Al_2O_3 is progressively converted to AlF_3 or AlO_xF_y. This conversion is predicted based on the published literature by DuMont and George, in which HF is used as a surrogate for fluorine exposure [**58**]. The IR band at 775 cm^{-1} is assigned to the linkage O-H…..F of Iron oxide-hydroxide. This assignment follows the published literature of Sundaram et al. [**59**]. The band in the 993-1025 cm^{-1} range is assigned to short-range metal silicates. The 975 cm^{-1} to 1018 cm^{-1} band is assigned to short-range ordered aluminosilicates (Si-O-Al) in the published literature [**60-61**]. The lone pair interaction of nitrogen in the H_2FN complex with H-F, H_2FN....H-F, is assigned at 525 cm^{-1}. According to the literature, this N....H-F interaction is strong, and the basicity of the nitrogen lone pair increases. The symmetric stretching frequency of N-F is assigned at 910 cm^{-1}. This peak appears as a shoulder in the range of 993 cm^{-1} to 1025 cm^{-1} [**62**].

3.3 Elemental analysis

The presence of C, H, and S in experimental soil is determined twice using the elemental analyser. The % C and H in the soil are 0.35±0.04 and 0.02±0.03, respectively. Elemental sulfur is not detected in the soil. This % of C in the elemental analysis is consistent with the thermal analysis. Various researchers have found that moisture and crystal water in inorganic

compounds are not accurately determined [**63**]. Hence, there is a discrepancy between the % H found in elemental analysis and the soil moisture content.

3.4 Thermal analysis

3.4.1 TG-DSC analysis

The soil mass loss curve as a function of temperature is shown in **Fig.3a**.

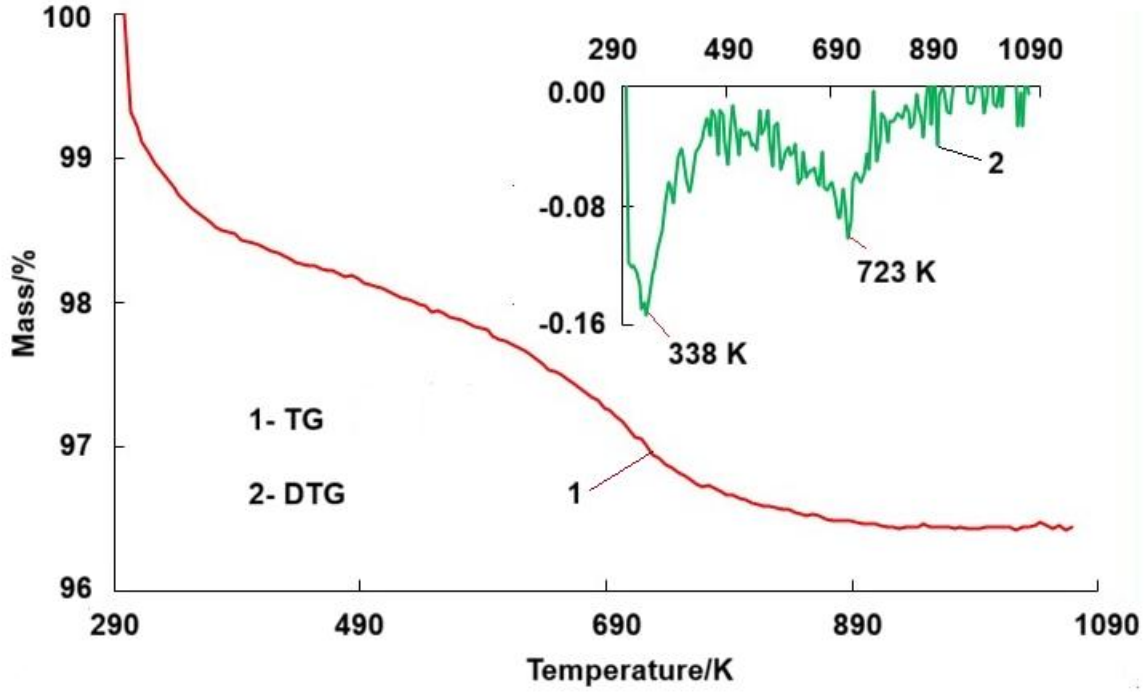


Fig.3a TG-DTG curve of the original soil

The exact temperature at which mass loss occurs cannot be readily determined from this TG curve. The DTG curve of soil is shown in **Fig.3a**. In this DTG curve, several sharp peaks are observed. Of these, two prominent peaks are at 338 K and 723 K. The mass loss at 338 K is 1.20%. This mass loss is due to the soil's moisture content, i.e., loosely bound water. In addition to moisture (loosely bound water), soil also contains bound water. This bound water is determined from the total mass loss in the 338 K to 473 K temperature range. The % of bound water in the soil is 0.60. A minor peak is observed at 473 K in the DTG curve. Three minor peaks, 388 K, 418 K, and 473 K, are observed in the temperature range 338 K to 473 K. There are three types of minerals present in this examined soil: AlF_3 or AlO_xF_y, Iron oxide-hydroxide, and silicates, which are confirmed from the FTIR spectrum. This may explain the three minor peaks in the DTG curve during the loss of tightly bound water from these three minerals in the soil. The temperature range for determining bound water in soil, as reported by Wang et al., is 378-473 K [**64**].

The physically bound water in Iron oxide-hydroxide minerals was lost at 388 K. Balek and Subrt reported dehydration of γ-FeOOH (lepidocrocite) at 393 K [**65**]. Dehydration of $AlF_3.xH_2O$ occurs at 418 K. Yang et al. reported that dehydration proceeds in a one-step process at ~413 K, as shown below [**66**].

$$AlF_3.3H_2O \xrightarrow{\sim 413\ K} AlF_3 + 3H_2O$$

The dehydration of silicate minerals occurs at 473 K. Rodriguez et al. reported that calcium silicate hydrate undergoes dehydration at 473 K. This dehydration temperature increases with increasing calcium-to-silicate ratio [**67**].

Determining soil organic carbon (SOC) in soil is essential because soil fertility depends on it. Many methods have been developed to determine SOC, but none provide as high a level of quantitative accuracy as the SOC method. The thermogravimetric method for determining SOC in soil is based on the following two equations [**68**].

$$SOC\ (present\ in\ soil) = 1.18 \times TML_{603} - 0.05 \quad (6)$$

$$SOC\ (present\ in\ soil) = 1.48 \times TML_{623} - 0.08 \quad (7)$$

TML_{603} stands for total mass loss at 603 K, and TML_{623} stands for total mass loss at 623 K. This mass loss is confirmed by thermogravimetric (TG) analysis. The SOC calculated using the above two equations is highly reliable and accurate. Many researchers have established this result through elemental analysis [**69**]. The % mass loss at 603 K and 623 K is 2.25 and 2.33, respectively. The mass loss percentages after dehydration at 603 K and 623 K are 0.45 and 0.53, respectively. The % SOC in the soil is calculated using equations (5) and (6), with values of 0.26 and 0.35, respectively. The % C present in the soil is determined experimentally to be 0.35 ± 0.04, by elemental analysis (C, H, S). The experimentally determined % C values coincide well with the calculated values from equation (7). The clay content in soil can be calculated using this equation provided by Siewert [**68**].

$$Clay = 4 \times TML_{393} + 9.8 \quad (8)$$

TML_{393} signifies total mass loss at 393 K. It is known that clay is a combination of tightly bound water, silica, and alumina or magnesia, or both alumina and magnesia. It also contains potassium, sodium, and calcium. The calculated clay content in the examined soil is 54.20%.

This conversion equation calculates the soil organic matter (SOM) from SOC.

$$SOM = 1.724 \times SOC \quad (9)$$

However, the conversion factor 1.724 used in the equation above does not yield accurate results. Many researchers used 2 as the conversion factor [**70**]. The SOM can be calculated using the equation provided below.

$$SOM = 2.0 \times SOC \quad (10)$$

The % of SOM present in the soil is 0.70. Sandy agricultural rice fields in northeast Thailand contain SOC ranging from 0.03% to 3.12% [**71**]. The heat flow-temperature graph is shown in **Fig.3b**.

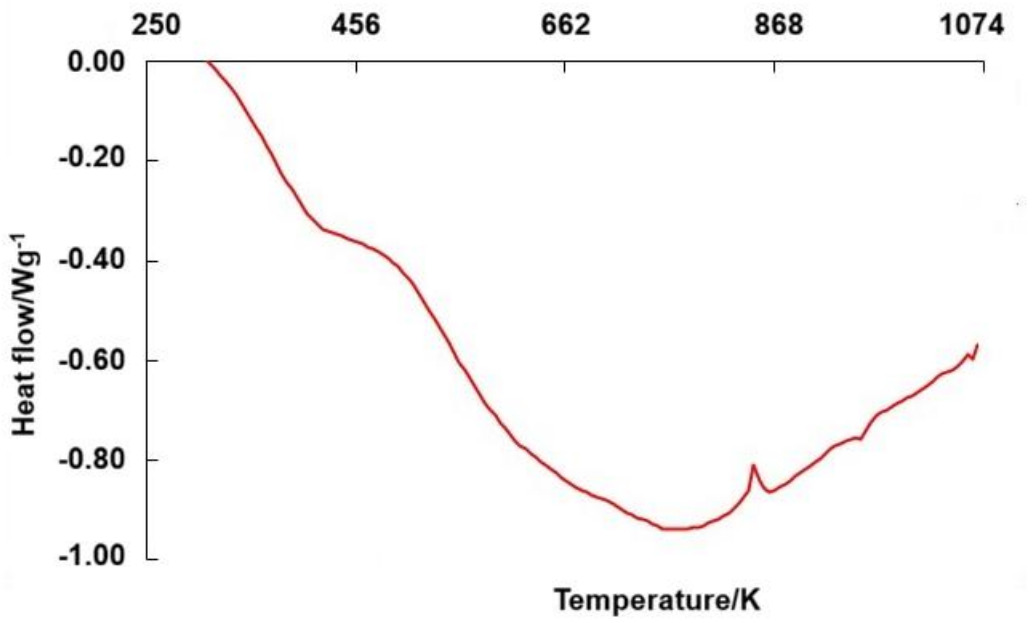


Fig.3b Heat flow as a function of the temperature of the original soil

Thermal analysis can be used to calculate soil thermal conductivity. This conductivity can be calculated from the soil temperature difference (Δθ) between times t_1 and t_2. This temperature difference in soil (Δθ) is directly proportional to the time ratio (t_2/t_1). The mathematical expression can be written as below [**72**].

$$\Delta\theta = \frac{\emptyset}{4\pi k} log\left(\frac{t_2}{t_1}\right) \quad (11)$$

Taking logs on both sides of the above equation and simplifying.

$$\log(\Delta\theta) = log\left(\frac{\emptyset}{4\pi k}\right) + log\left\{log\left(\frac{t_2}{t_1}\right)\right\} \quad (12)$$

Where $\emptyset$ is the heat capacity, and k is the thermal conductivity. A graph is plotted between $\log(\Delta\theta)$ and $log\left\{log\left(\frac{t_2}{t_1}\right)\right\}$. A straight-line: Y = m$x$+$c$, $Y = 2.5167x + 1.0427$, $R^2 = 0.9851$, which is observed with an intercept of 1.0427. The thermal conductivity k is calculated from the intercept of the equation. The thermal conductivity increases with temperature, reaches a maximum at ~318 K, and then decreases. The thermal conductivity-temperature graph is shown in **Fig.3c**.

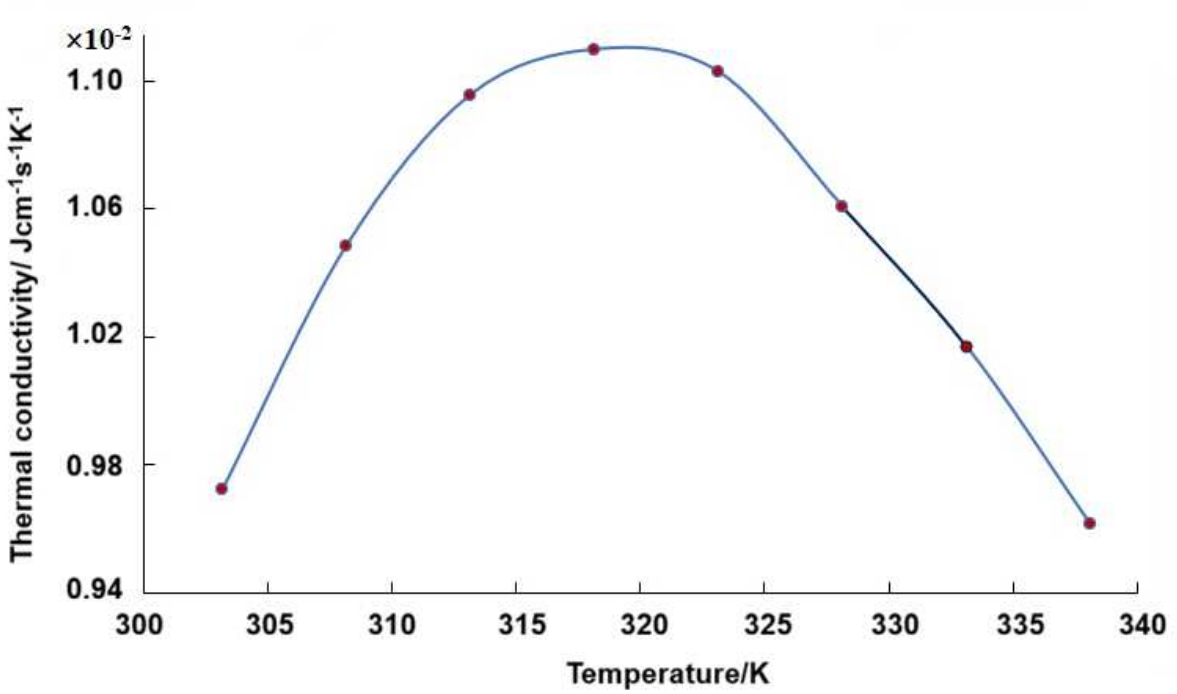


Fig.3c Thermal conductivity as a function of temperature of the original soil

3.4.2 Comparison of the chemically treated and the original soil

As with the original soil, the exact temperature at which moisture loss occurs cannot be readily determined from the TG curve of the chemically treated soil. The moisture loss from Acid- and alkali-treated soil is determined from the DTG curves, occurring at 323 K (0.64%) and 322 K (0.50%), respectively. Because several minor and major peaks are observed in the DTG curve, the temperature at which bound water is removed from the chemically treated soil is not readily determined. The DSC curve of the chemically treated soil represents one distinct endothermic peak for the removal of bound water. The bound water from the acid- and alkali-treated soil is removed at 428 K (0.48%) and 427 K (0.50%), respectively. This indicates that the % moisture loss (more than 50%) and bound water loss (~20%) are lower than in the original soil. The TG-DTG and DSC curves for the acid- and alkali-treated soil are shown in Supplementary **Fig. S2(a-d)**, respectively.

The thermal conductivity of the chemically treated soil was calculated using Equation 12, and the thermal conductivity graph was plotted as a function of temperature. Thermal conductivity increases with temperature, reaching a maximum at ~308 K for acid-treated soil and 312 K for alkali-treated soil, then decreasing. The thermal conductivity and temperature graph is displayed in **Fig.S2(e-f)**. The FTIR spectrum of alkali-treated soil confirms that fluoride-containing aluminosilicates and Si-O-Al minerals are completely/ partially removed from the

soil during alkali leaching. So, the maximum thermal conductivity temperature of the alkali-treated soil is higher than that of the acid-treated soil. The maximum thermal conductivity temperature is less than that of the original soil. This also aligns with the optical bandgap graph, which shows that the chemically treated soil has a lower optical bandgap than the original soil.

3.4.3 Specific heat capacity of soil

The soil's C_P is determined in an N_2 atmosphere at a heating rate of 2K min^{-1}. The temperature-versus-specific heat capacity graph is shown in **Fig.3d** over the temperature range of 267 K to 339 K.

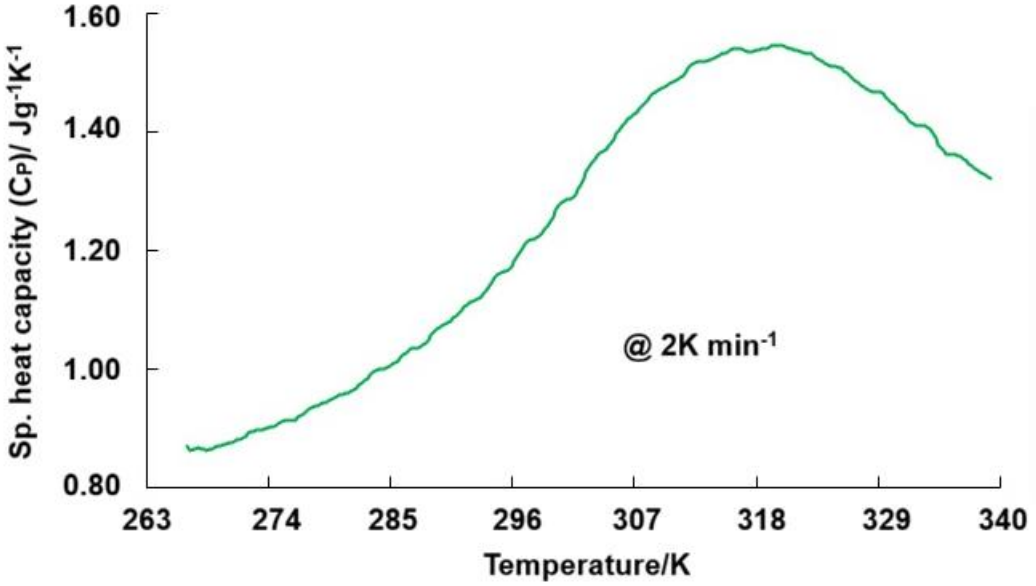


Fig.3d Specific heat capacity as a function of temperature of the original soil.

The C_P increases with increasing soil moisture content. The C_p of sandy-type soil is ~ 0.85 $Jg^{-1}K^{-1}$ at ~2.5% moisture content. The composition of sandy soil is 90% sand, 5% silt, and 5% clay. The C_p of clay soil is ~1.20 $Jg^{-1}K^{-1}$ at ~2.5% moisture content. The composition of the clay soil is 20% sand, 22% silt, and 58% clay. The C_p and composition of sandy and clay soil are collected from the published manuscript [**73**]. The C_p of this examined soil at room temperature is 1.22 $Jg^{-1}K^{-1}$ at 1.80% moisture content. The C_p value of the examined soil is ~ 70% higher than that of sandy soil and almost the same as that of clay soil. The examined fluoride-contaminated soil contains ~34% silicon and 54% clay. In comparing the C_p of the examined soil and the above two types of sandy and clay soil, the soil absorbs more heat than the other two. The moisture content of soil plays a vital role in its C_P. Wang et al. reported the C_P of the soil heated at 378 K and 473 K. The C_p of soil preheated at 378 K is 0.75 $Jg^{-1}K^{-1}$ at 293 K. This preheated soil contained organic matter, minerals, and tightly bound water (0.14%

to 0.85%). The C_p of preheated soil at 473 K is 0.74 $Jg^{-1}K^{-1}$ at 293 K. This preheated soil contained organic matter and minerals but did not contain tightly bound water. The C_P value of the above soil is collected from the published literature [**74**]. The C_p of the examined soil sample is ~60% higher than that of the above moisture-free preheated soil. Wang et al. also reported that the organic matter-free preheated soil at 378 K and 473 K shows almost same C_p, 0.74 $Jg^{-1}K^{-1}$ (378K) and 0.73 $Jg^{-1}K^{-1}$ (473K), values as compared with the presence of organic matter in soil at 293 K. Wang et al. also reported that the C_p of preheated soil at 473 K found almost constant value, ~ 0.74 $Jg^{-1}K^{-1}$ at 293K, with the increase of clay %, 10 to 50, in soil. In contrast, the C_p of organic matter-free preheated soil at the same temperature ranges from ~0.72 $Jg^{-1}K^{-1}$ to ~0.76 $Jg^{-1}K^{-1}$, increasing with clay % in the soil. In this preheated soil, tightly bound water was not present. With an increase in clay % from 10 to 50, the C_p of preheated soil at 378 K varies from 0.74 $Jg^{-1}K^{-1}$ to 0.78 $Jg^{-1}K^{-1}$ in the presence of organic matter. In comparison, the C_p of organic matter-free preheated soil at 378 K varies from 0.73 $Jg^{-1}K^{-1}$ to 0.74 $Jg^{-1}K^{-1}$ at 293 K. This indicates that clay content in soil is not a significant factor in C_p. The presence of tightly bound water in the range of 0 % to 1% varies the C_p value by 8%, from 0.72 $Jg^{-1}K^{-1}$ in 0% tightly bound water.

The relationship between the temperature rise (ΔT) and the time interval t_1 (initial time) and t_2 (final time) is given below.

$$\Delta T = \left(\frac{\emptyset}{4\pi k}\right) ln\left(\frac{t_2}{t_1}\right) \qquad (13)$$

After rearranging the above equation

$$\left(\frac{4\pi k}{\emptyset}\right)\Delta T = lnt_2 - lnt_1$$

$$lnt_2 = lnt_1 + \left(\frac{4\pi k}{\emptyset}\right)\Delta T \qquad (14)$$

k is the thermal conductivity, and ∅ is a heat source. The ∅ is expressed in Jg^{-1}. The graph is plotted between lnt_2 and ΔT. The straight-line equation Y = mx + c, $Y = 0.0174x + 6.8386$, is obtained. The slope and intercept of this straight line are 0.0174 and 6.8386, having R^2 = 0.9722. The calculated thermal conductivity (k) is plotted against C_P. This graph is shown in **Fig.3e**.

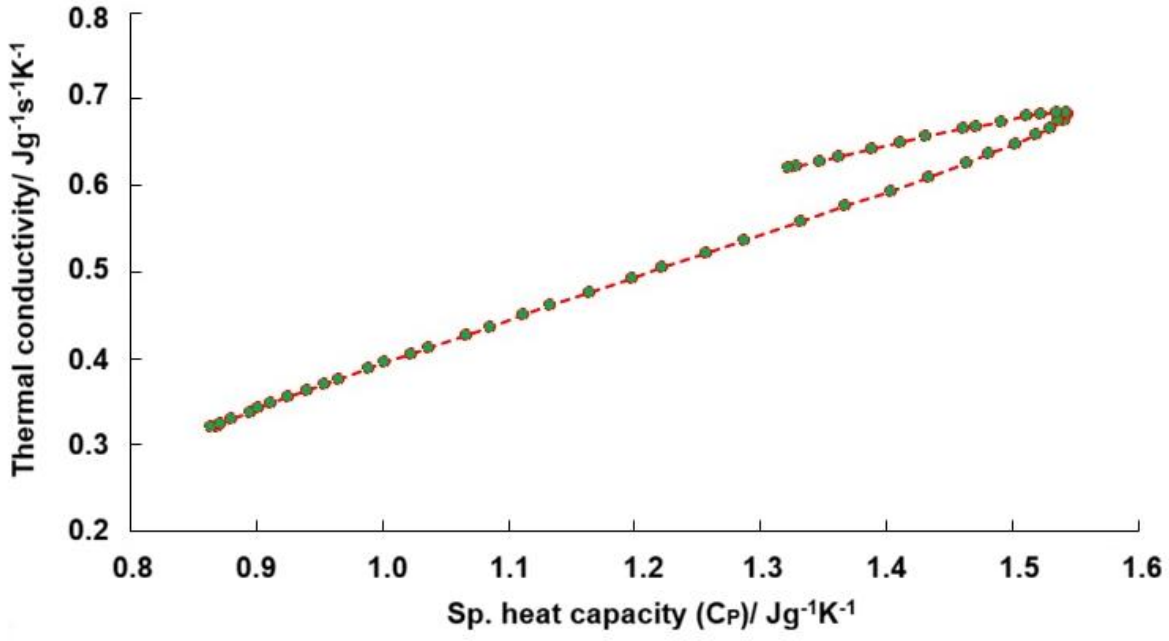


Fig.3e The C_P versus thermal conductivity of the original soil.

The thermal conductivity increases with specific heat capacity up to C_p = 1.54 $Jg^{-1}K^{-1}$, then decreases. The graph of C_P versus temperature also shows a similar trend.

3.5 NMR analysis

3.5.1 Original soil

^{19}F NMR spectrum

The ^{19}F NMR spectrum of the examined soil sample is shown in **Fig.4a**.

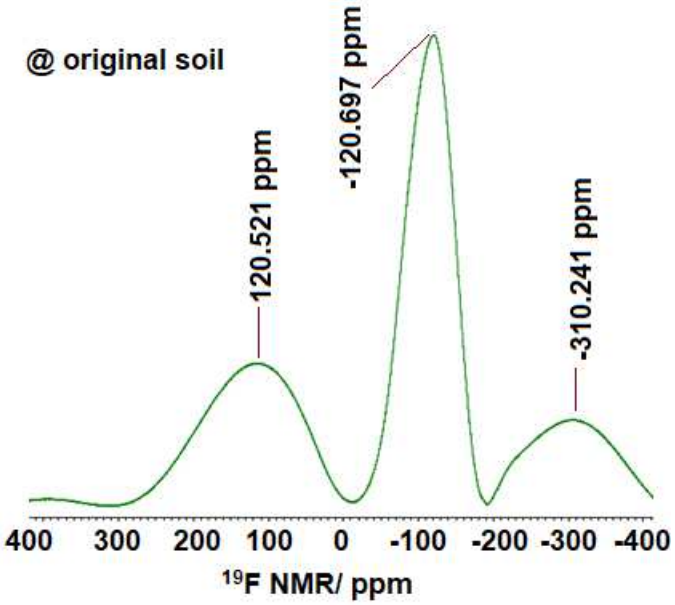


Fig.4a ^{19}F NMR spectrum of the original soil

The ^{19}F NMR spectrum at ~ -120 ppm is assigned to the hydrated zeolite containing fluoride minerals of Si and Al, along with free fluoride ions. According to the published literature on

fluorine chemical shifts, the examined soil sample contains a fluoro-aluminium complex. This complex contains at least 4 fluoride ions per aluminium ion. This ^{19}F NMR peak is observed upon reacting aqueous aluminium (III)chloride with ammonium fluoride in a 1:4 ratio. The ^{19}F NMR spectrum peak is not observed below a 1:4 ratio of aluminium chloride to ammonium fluoride. All the above interpretations are based on the published literature [**75**]. This signal is very broad, from -30 ppm to -190 ppm. This is due to the movement of fluorine atoms among Si, Al, and Fe compounds present in the soil. This exchange of the fluoride ligand among the compounds can occur in various ways, such as silicon fluoride in the form of SiF_4, SiF_5^-, SiF_6^{2-}, etc. However, researchers find it challenging to accurately identify these compounds [**76**]. The IR spectrum of the soil also confirms the presence of fluoride minerals. It is possible to avoid the broad signal arising from the motion of the fluorine atoms by measuring the NMR spectrum at low temperatures. However, this facility is not available here. It is known that the ^{19}F NMR signals of $AlF_3.3H_2O$ are observed at approximately 60 ppm and 110 ppm, along with other signals. The ^{19}F NMR signal of the zeolite containing octahedral $AlF_3.3H_2O$ is ~120 ppm [**77**]. The ratio of the signals between -120.697 ppm and 120.521 ppm is 3.13.

^{29}Si NMR analysis

The ^{29}Si NMR spectrum of the original soil sample is shown in **Fig.4b**.

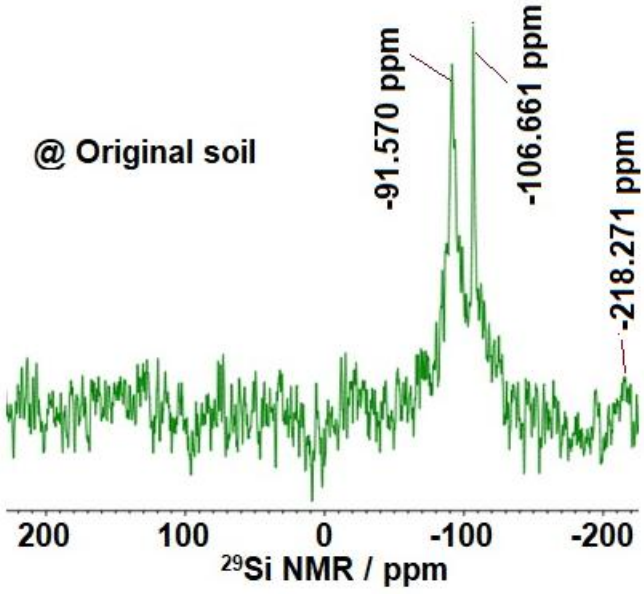


Fig.4b ^{29}Si NMR spectrum of the original soil

The signal at ~-91 ppm in the original soil resembles that of amorphous silica in ZSM-5 zeolite, $Si(OSi)_2(OH)_2$ [**78**]. The signal for the examined soil at -106 ppm indicates the presence of more than 1% aluminium, similar to that of ZSM-5 zeolite [**79**]. The signal at ~-106 ppm and

its correlation signal at ~-218 ppm indicate covalent bonds between Si atoms in the soil, similar to those in ZSM-5 zeolite [**80**]. In these covalent bonds, a Si atom is attached to four other Si atoms through O bonds [**81**].

^{27}Al NMR analysis

The ^{27}Al NMR spectrum of the original soil is displayed in the range of -300 ppm to 300 ppm in the **Fig.4c**.

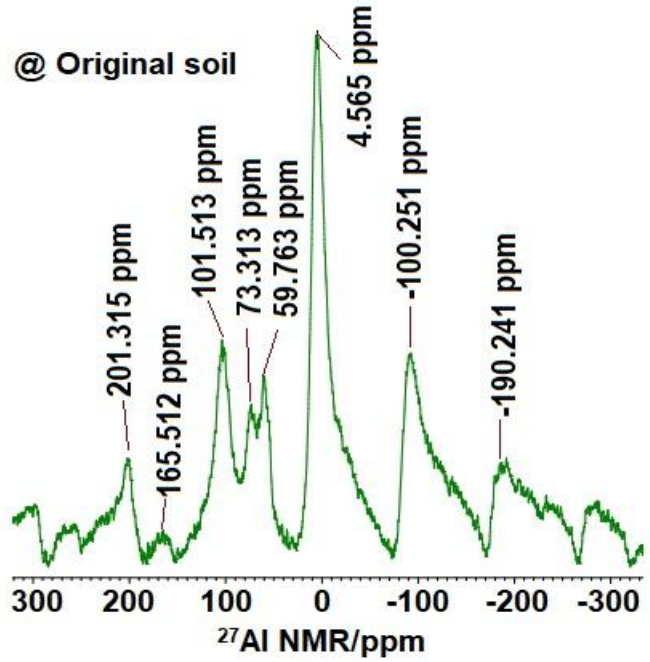


Fig.4c ^{27}Al NMR spectrum of the original soil

The signals at ~4.5 ppm and ~59 ppm reflect different hydration proportions in H-ZSM-5/NH_4-ZSM-5 FLD-synthesized zeolites [**82-83**]. The signal intensity at ~4.5 ppm is high, indicating that the aluminium species with a fluoride concentration greater than 10% is octahedrally coordinated. This aluminium species resembles the dehydrated H-ZSM-5/NH_4-ZSM-5 FLD zeolites/F in $Al_2O_3\{Al(O_{6-n}F_n)\}$, which exhibit varying degrees of hydration [**77**]. The low-intensity signal at ~59 ppm, compared to ~4.5 ppm, indicates the presence of tetrahedral-coordinated aluminium species in soil. This unsplit signal signifies that the dehydrated H-ZSM-5/NH_4-ZSM-5 FLD zeolites are excessively hydrated [**82-83**]. The signal at ~73 ppm of the examined soil resembles the compound $AlO_yN_{4-y}, 0 \leq y \leq 4$. This compound is associated with a mixed tetrahedral structure in which chemical shifts and/or quadrupole coupling constants exhibit fluctuations [**84**]. The original soil contains various proportions of calcium and aluminium oxides: $3CaO.Al_2O_3$ (C_3A) in CaO to Al_2O_3 ratio 3.0 or $C_{12}A_7$, $12CaO.7Al_2O_3$, type having CaO to Al_2O_3 ratio 1.7. The structure of these oxides is speculated as follows. The

AlO_4 tetrahedral aluminium atoms of the C_3A-type compound form a six-membered ring, and these tetrahedral aluminum atoms in the C_3A-type compound are of two types. Compared to this, there are also two types of Al atoms in the $C_{12}A_7$ type compound. One of the Al atoms is tetrahedral and is bridged with $[AlO_2]^-$ groups, while other tetrahedral Al atoms contain one non-bridged oxygen atom. These Al structures in calcium and aluminium oxide compounds are interpreted from the ~101 ppm signal position in ^{27}Al NMR spectra, as described by Müller et al. [**85**]. The ~165 ppm signal in the soil resembles that of hydrated H-ZSM-5 (Si/Al = 40), and it's washed with ammonium hexafluorosilicate. After washing, the silicon-to-aluminium ratio decreases from 40 to 15. The soil contains H-ZSM-5/AHFS-HZSM-5 type minerals. This signal disappears in dehydrated form [**82**]. The ~200 ppm signal observed in the examined soil resembles that of dehydrated H-BEA-type zeolite [**86**]. So, the soil contains the oxides of silicon, sodium, and aluminium. The ~-190 ppm signal of the soil resembles that of the non-hydrated zeolite H, Na-Y. Hence, the soil contains the oxides of sodium, aluminium, and silicon in varying proportions [**87**]. The broad signal at -100.251 ppm resembles that of the zeolite H-β, which is dealuminated by ammonium hexafluorosilicate (AHFS), $(NH_4)_2SiF_6$. The dealuminated zeolite is fully hydrated, $(NH_4)_3AlF_6$ [**88**].

3.6 ISE measurement (Fluoride)

The fluoride ion was measured using an ISE in an acid-leaching solution at different pH levels, maintained with 0.1 N NaOH solution. **Fig. 5** shows the fluoride ion concentration at different pH levels.

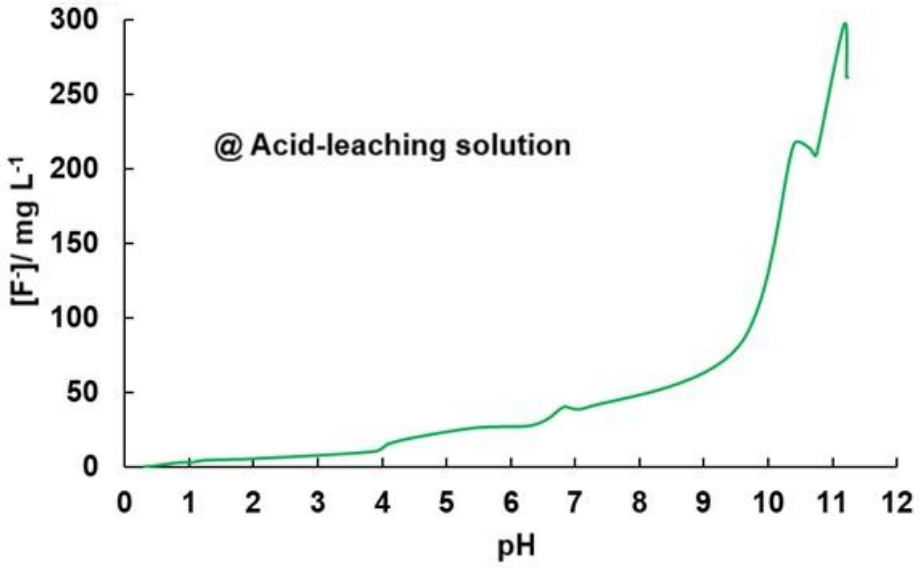


Fig.5 Fluoride ion measurement of acid leaching solution

The acid-leaching filtrate was treated with $Ca(OH)_2$, and fluoride was measured at different pH levels using a fluoride ISE. The fluoride concentration increases with increasing pH. In an alkaline medium, fluoride is released by OH^-, i.e., the OH^- ion replaces the exchangeable fluoride present in the acid-leaching solution.

The ^{27}Al NMR acid-treated residue indicates that the signal at ~165 ppm remains absent. So, the fluoride-containing zeolite AHFS-HZSM-5 was leached from the soil. The leached fluoride undergoes exchangeability by OH^- to form CaF_2.

$$[AHFS-HZSM-5]xF_2 + OH^- \rightarrow [AHFS-HZSM-5]xOH^- + xF^-$$

The $pK_b[Ca(OH)_2] = 1.37(pK_{b1}) - 2.43\ (pK_{b2})$

The maximum fluoride concentration occurs at pH = 11.17, where it is 296 mg L^{-1}; further increases in pH to 11.23 reduce the fluoride concentration to 261 mg L^{-1}. This may be due to the formation of CaF_2 precipitate.

$$Ca^{2+} + xF^- \rightarrow xCaF_2 \text{ (precipitate)}$$

The pH of the solution was further reduced to 11.03, with a fluoride concentration of 1.22 mg L^{-1}, and the precipitate continued to form. The $[F^-]$ was reduced to less than 10^{-4} mg L^{-1} (not detected) at pH 8.59.

3.7 Morphology analysis

The morphologies of the original, acid-treated, and alkali-treated soils are shown in **Fig.6**.

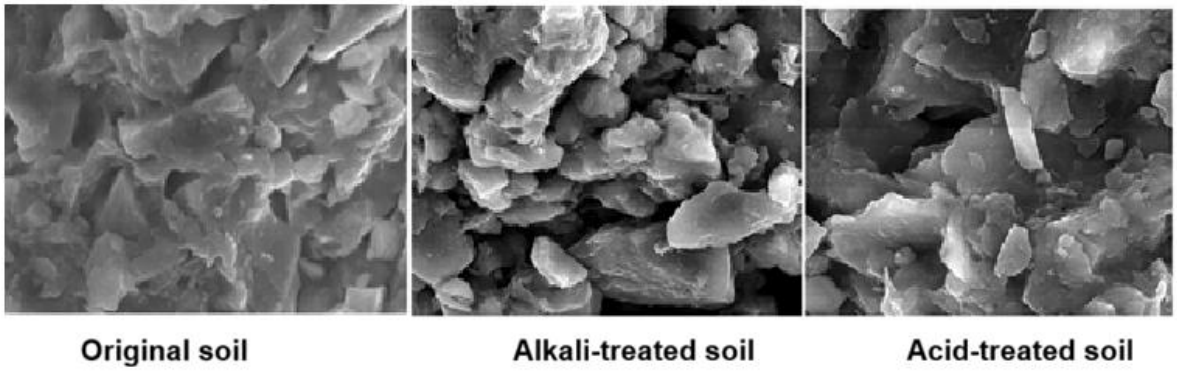


Fig.6 SEM images of the original, acid- and alkali-treated soil

The morphology of the original and acid-treated soils is similar, but the alkali-treated soil appears much denser. The EDAX of the original, acid-treated, and alkali-treated soils contain the following elements in the order provided below. The EDAX was measured at four different sites in the soil, and the average was calculated.

Original soil: Oxygen > Silicon > Aluminium > Iron > Potassium > Magnesium

Acid-treated soil: Oxygen > Silicon > Aluminium > Iron > Potassium > Magnesium > Calcium

Alkali-treated soil: Oxygen > Silicon > Aluminium > Iron > Potassium > Magnesium > Calcium

The quantitative measurements of fluorine and carbon vary across all three soil types. This may be because the light elements were not identified correctly.

4 Discussion

4.1 Comparison of the original and chemically treated soil (FTIR measurement)

The FTIR spectra of the acid- and alkali-treated soil are shown in Supplementary **Fig.S3a and S3b**, respectively. The IR band of acid-treated soil is almost similar to that of the original soil. The transmittance % of the bands at 521cm^{-1}, 1027 cm^{-1}, and 1076 cm^{-1} of the acid-treated soil is less than that of the original soil, while the band at 688 cm^{-1} is higher than that of the untreated soil. This indicates that some fluoride compounds, such as AlF_3 or AlO_xF_y, are partially removed during acid treatment. In the alkali treatment, the % transmittance of the IR bands at 691 cm^{-1} and 789 cm^{-1} is higher than in the untreated soil. This implies that, in addition to AlF_3 or AlO_xF_y compounds, other fluoride compounds, such as fluoride-containing iron oxide-hydroxide, are particularly removed from the original soil during alkali treatment. The bands at 910 cm^{-1}, 1004 cm^{-1}, and 1029 cm^{-1} remain absent in alkali-treated soil. The short-range-ordered aluminosilicates (Si-O-Al) might be completely/ partially removed during this alkali treatment.

4.2 Thermal analysis

The heat flow in terms of C_P can be expressed as

$$\frac{dH}{dT} = m \times C_p \times \Delta T \qquad (15)$$

The heat flow versus temperature graph indicates that heat flow is negative. The C_P versus temperature graph indicates that C_P is positive, as shown by expanding equation (15) as follows.

$$\frac{dH}{dT} = (m_2 - m_1) \times C_p \times (T_2 - T_1) \qquad (16)$$

Let the initial mass of soil be m_1 at temperature T_1. The soil mass changes from m_1 to m_2 as the temperature changes from T_1 to T_2. The temperature difference, ΔT ($T_2 - T_1$), is positive as $T_2 > T_1$.

The thermogravimetric analysis indicates the soil mass decreases as the temperature increases. This mass decrease is due to moisture removal, tightly bound water, and other organic matter in the soil. Hence, the mass difference, Δm ($m_2 - m_1$), is negative as $m_2 < m_1$. Substituting the

convention of heat flow, the mass difference (Δm), and the temperature difference (ΔT) in equation (16).

$$-\frac{dH}{dT} = (-\Delta m) \times C_p \times (\Delta T) \qquad (17)$$

By rearranging the above equation

$$C_p = \frac{\frac{dH}{dT}}{\Delta m \times \Delta T} \qquad (18)$$

Equation (18) indicates that C_P is positive and endothermic.

4.3 Comparison of the C_P of the chemically treated and original soil

Supplementary **Fig. S4** shows the C_P of the chemically treated soil as a function of temperature. The C_P of the chemically treated soil is lower than that of the original soil because mineral leaching occurs during treatment. Similarly, the C_P of the alkali-treated soil is less than that of the acid-treated soil due to excessive leaching of minerals in the alkali process compared to acid treatment. This excessive mineral leaching during the alkali process, compared to the acidic process, is confirmed by the FTIR spectrum. The maximum C_P of the acid-treated and alkali-treated soil is 0.99 $Jg^{-1}K^{-1}$ at 305 K and 0.72 $Jg^{-1}K^{-1}$ at 312 K, respectively. The maximum C_P of the original soil is 1.55 $Jg^{-1}K^{-1}$ at 320 K.

4.4 Comparison of the NMR analysis

4.4.1 ^{19}F NMR analysis

After acid treatment, the ^{19}F NMR signal shifted to 77.208 ppm. Fischer et al. reported that the center of gravity of the ^{19}F NMR signal shifted from 9 ppm to 33 ppm as the fluorination of the γ-Al_2O_3 surface increased from 0.8% to 12% [**77**]. So, the zeolite containing fluoride of alumina converted from octahedral to tetrahedral $AlF_3 \cdot H_2O$ with high fluorination after acid treatment. The ratio of the signals between -133.694 ppm and 77.208 ppm is 2.14. The abundance ratio of the signal is 0.99 times that of the original soil (before acid treatment). This is due to the leaching of excess fluoride ions from the zeolite during acid treatment. This is confirmed by the ISE measurement of fluoride ions. The ^{19}F NMR spectrum after acid treatment is displayed in supplementary **Fig.S5a**.

After alkali treatment, the ^{19}F NMR signal of octahedral and tetrahedral hydrated AlF_3 at 60 ppm and 110 ppm remains absent. This may be due to removal from the zeolite, but the IR band at 691 cm^{-1} after alkali treatment indicates that fluorination of Al_2O_3 is present in the zeolite (AlO_xF_y). The signal at -118. 313 ppm in alkali-treated soil is nearly equal to that in acid-treated and untreated soils. The ^{19}F NMR spectrum after alkali-treatment is displayed in Supplementary **Fig.S5b**.

4.4.2 ^{29}Si NMR analysis

After acid-treatment, the signals of ^{29}Si NMR remain intact. This indicates that amorphous silica in ZSM-5 zeolite cannot be leached. The ^{29}Si NMR spectrum after acid-treatment is displayed in Supplementary **Fig.S5c**.

After alkali treatment, the ^{29}Si NMR signal at –106.295 ppm remains intact, as in untreated and acid-treated soil. The signal at –91.570 ppm of the untreated soil split into –90. 545 ppm and –85. 197 ppm. The signal at -85.197 ppm might be due to excessive hydration of silicon in alkali treatment. The ^{29}Si NMR spectrum after alkali-treatment is displayed in Supplementary **Fig. S5d**.

4.4.3 ^{27}Al NMR analysis

After acid treatment, the ^{27}Al NMR spectrum shows signal positions similar to those of the original soil but with different abundances. The signal at ~60.404 ppm refers to tetrahedral coordinated aluminium species, while ~73.771 ppm refers to the aluminium compound ($AlO_yN_{4-y}, 0 \leq y \leq 4$) having a mixed tetrahedral structure. The ratio of the abundance between the tetrahedral structure and the mixed tetrahedral structure of aluminium is 0.84 times greater than that of the original soil. This indicates that some of the mixed tetrahedral structure of aluminium, $AlO_yN_{4-y}, 0 \leq y \leq 4$, was leached during acid treatment. The signal at ~101.513 ppm refers to the tetrahedral Al atoms in bridged, $[AlO_2]^-$, and non-bridged oxygen atoms. The abundance of the signal at 104.055 ppm in acid-treated soil is much less than in the original soil. The ratio of tetrahedral Al species to the aluminum in bridged and non-bridged oxygen atoms is less than 0.70 times in the original soil compared to the acid-treated soil. This indicates that the tetrahedral Al in the bridged and non-bridged structures was leached from the soil during acid treatment. The signal at ~165 ppm corresponds to the hydrated H-ZSM-5/AHFS-HZSM-5-type minerals present in soil. This signal disappears in acid-treated soil. This indicates that the above minerals in soil are in a dehydrated form [**82**]. The ^{27}Al NMR spectrum of the acid-treated soil is displayed in the supplementary **Fig.S5e**.

After alkali treatment, the ^{27}Al NMR spectrum shows signal positions similar to those of the original soil but with different abundances. The ratio of the abundance between the tetrahedral structure and the mixed tetrahedral structure of aluminium is 1.34 times greater than that of the original soil and 0.5 times greater than that of the acid-treated soil. This indicates that some of the mixed tetrahedral structure of aluminium, $AlO_yN_{4-y}, 0 \leq y \leq 4$, was leached during alkali treatment. This alkali leaching is much greater than that in acid-leached soil. The ratio of tetrahedral Al (59.959 ppm) species and the aluminium in bridged and non-bridged oxygen

atoms (100.192 ppm) is less than 1.15 times in the original soil compared to the alkali-treated soil. This indicates that the tetrahedral Al in the bridged and non-bridged structures was leached from the soil during alkali treatment. This leaching is much greater than that of acid leaching. The signal at ~165 ppm corresponds to the hydrated H-ZSM-5/AHFS-HZSM-5-type minerals present in soil. This signal disappears in acid-treated soil. This indicates that the above minerals in soil are in a dehydrated form [**82**]. The ^{27}Al NMR spectrum of the alkali-treated soil is displayed in the supplementary **Fig.S5f**.

4.5 FTIR analysis of the isolated product

The acid-leached solution was used to measure fluoride ions at different pH levels, and the pH was adjusted using 1 M $Ca(OH)_2$. During pH adjustment, a precipitate formed, and the fluoride meter could not detect fluoride ions. The precipitate was filtered and dried in a silica gel-containing desiccator. The FTIR spectrum of the fluoride-containing isolated product is shown in the **Fig. 7.**

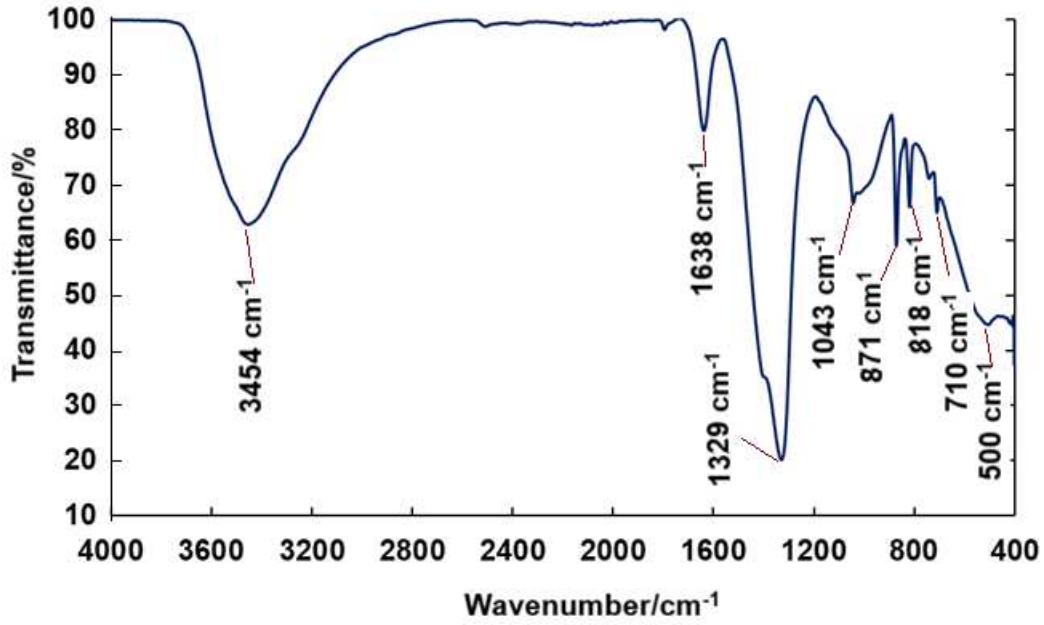


Fig.7. FTIR spectrum of the precipitate of acid-leached fluoride solution.

The IR band at 710 cm^{-1} is assigned to the deformation vibrations of Si-O-Al/Si-O-Si [**89**]. The IR band at 818 cm^{-1} is assigned to the Al-O asymmetric vibration of $[AlO_4]^{5-}$, while 1043 cm^{-1} is assigned to the Al-O stretching vibration in $(OAlF)_2$ [**90**]. A broad band at 3454 cm^{-1} is assigned to the vibrations of the -OH group along with Si, Al, and Ca ions [**91**]. The band at 871 cm^{-1} is assigned to tetrahedral AlO_4, and the peak at 499 cm^{-1} is assigned to α-Al_2O_3, which

is the region of octahedra AlO_6 [**92**]. The bands at 1328 cm^{-1} and 1637 cm^{-1} are assigned to the antisymmetric stretching mode of NO_3^- and the bending mode of water, respectively [**93**]. This compound may be hydrated calcium nitrate.

5 Conclusion

The soil was collected using a screw auger, air-dried, sieved, and stored in a polythene jar. Various spectroscopic measurements (UV-Vis-NIR, FTIR, ^{19}F NMR, ^{27}Al NMR, ^{29}Si NMR, SEM-EDAX) and thermal measurements (TG-DSC and C_P) were carried out for the original soil, acid-treated soil, and alkali-treated soil. The reflectance of the acid-treated soil is slightly greater than that of the other types of soil (original and alkali-treated soil). ^{27}Al NMR measurements show that the original soil contains H-ZSM-5/NH_4-ZSM-5 types of zeolites. It also contains fluoride minerals such as $Al_2O_3\{Al(O_{6-n}F_n)\}$, and AlO_yN_{4-y}, $0 \leq y \leq 4$. Other NMR measurements, such as ^{29}Si and ^{19}F NMR, confirm that the minerals contain fluoride. Fluoride minerals are partially leached during acid and alkali treatments of the original soil. The fluoride-containing HZSM-5-AHFS is completely leached from the original soil, as confirmed by further ^{27}Al NMR spectra of the acid-treated soil. Fluoride ISE was used to measure the fluoride at different pH.$[F^-]$ The $[F^-]$ is 296 mg L^{-1} at pH 11.17; after that, the $[F^-]$ decreases and is not detected at pH 8.59. More work is needed to remove fluoride from other zeolites present in the acid-and alkali-treated soil.

Declarations

Conflict of Interest

The authors declare no conflicts of interest.

Author's contribution

The author, MB, did all the experiments. The author TS analysed the data and wrote the initial and final drafts of the manuscript.

Ethical Approval

No human or animal participants were used in this study.

Funding

No funding was received for conducting this study

Data Availability

All the extra data are included in the supplementary file.

Conflict of Interest

The authors declare no conflicts of interest.

Consent to Participate declaration: Not applicable

Consent to Publish declaration: Not applicable

Acknowledgement

Both the authors, TS and MB, thank the SAIF, DST-supported institute NMR facility at IISc for the NMR spectra. The authors also thank SAIF IIT Madras and SAIF Kochi for various measurements. The author MB thanks the P.G. Department of Chemistry for providing the necessary laboratory facilities.

Reference

1. Adeyeye OA, Xiao C, Zhang Z, Yawe AS, Liang X. Groundwater fluoride chemistry and health risk assessment of multi-aquifers in Jilin Qianan, Northeastern China. Ecotoxicology and Environmental Safety. 2021; 211: 111926. https://doi.org/10.1016/j.ecoenv.2021.111926.
2. Guissouma W, Hakami O, Al-Rajab AJ, Tarhouni J. Risk assessment of fluoride exposure in drinking water of Tunisia. Chemosphere. 2017; 177: 102-108. https://doi.org/10.1016/j.chemosphere.2017.03.011.
3. Asgari G, Ghalehaskar S, Moghaddam VK, Radfard M, Heidarinejad Z, Mohammadi AA, Faraji H. Monitoring and health risk assessment of fluoride in drinking water in Babol, Mazandaran Province, Iran. Desalination and Water Treatment. 2019; 165: 141–147. https://doi.org/10.5004/dwt.2019.24553.
4. Cengeloglu Y, Esengul K, Ersoz M. Removal of Fluoride from aqueous Solution by Using Bauxite Wastes. Separation and Purification Technology. 2002; 28: 81–86. https://doi.org/10.1016/S1383-5866(02)00016-3.
5. Mikkonen HG, van de Graaff R, Mikkonen AT, Clarke BO, Dasika R, Wallis CJ, Reichman SM. Environmental and anthropogenic influences on ambient background concentrations of fluoride in soil. Environmental Pollution. 2018; 242(Part B): 1838-1849. https://doi.org/10.1016/j.envpol.2018.07.083.
6. Hajduga N, Subramanian MP, Brown H, McNally R, Zohoori V, Rand V. Exposure to fluoride and risk of primary bone cancer: A systematic review. Bone. 2025; 190: 117320. https://doi.org/10.1016/j.bone.2024.117320.
7. Cross L. Fluoride: friend or foe? Exploring the effect of fluoride exposure on children's IQ scores. Evidence-Based Dentistry. 2025; 26: 137–138. https://doi.org/10.1038/s41432-025-01176-x.
8. Zhang Y, Gao Y, Liu X. Focus on cognitive impairment induced by excessive fluoride: An update review. Journal of Neuroscience. 2026; 558: 22-29. https://doi.org/10.1016/j.neuroscience.2024.08.011.
9. Joseph A, Rajan R, Paul J, Cherian KE, Kapoor N, Jebasingh F, Asha HS, Thomas N, Paul TV. The continuing crippling challenge of skeletal fluorosis –Case series and review of literature. Journal of Clinical and Translational Endocrinology: Case Reports. 2022; 24: 100114. https://doi.org/10.1016/j.jecr.2022.100114.
10. Veneri F, Vinceti M, Generali L, Giannone ME, Mazzoleni E, Birnbaum LS, Consolo U,

747 Filippini T. Fluoride exposure and cognitive neurodevelopment: Systematic review and
748 dose-response meta-analysis. Environmental Research. 2023; 221: 115239.
749 https://doi.org/10.1016/j.envres.2023.115239.
750 11. Jacks G, Bhattacharya P, Chaudhary V, Singh KP. Controls on the genesis of some
751 high-fluoride groundwaters in India. Applied Geochemistry. 2005; 20: 221–228.
752 https://doi.org/10.1016/j.apgeochem.2004.07.002.
753 12. Chae G-T, Yun S-T, Kim K, Mayer B. Hydrogeochemistry of sodium- bicarbonate type
754 bedrock groundwater in the Pocheonspa area, South Korea: water– rock interaction and
755 hydrologic mixing. Journal of Hydrology. 2006; 321: 326–343.
756 https://doi.org/10.1016/j.jhydrol.2005.08.006.
757 13. Ozsvath D. Fluoride concentrations in a crystalline bedrock aquifer, Marathon County,
758 Wisconsin. Environmental Geology. 2006; 50: 132–138.
759 https://doi.org/10.1007/s00254-006-0192-6.
760 14. Apambire WB, Boyle DR, Michel FA. Geochemistry, genesis, and health implications of
761 fluoriferous groundwater in the upper regions of Ghana. Environmental Geology. 1997;
762 33: 13–24. https://doi.org/10.1007/s002540050221.
763 15. Saxena VS, Ahmed S. Inferring the chemical parameters for the dissolution of fluoride
764 in groundwater. Environmental Geology. 2003; 43:731–736.
765 https://doi.org/10.1007/s00254-002-0672-2.
766 16. Saxena VS, Ahmed SA. Dissolution of fluoride in groundwater: a water-rock interaction
767 study. Environmental Geology. 2001; 40: 1084–1087.
768 https://doi.org/10.1007/s002540100290.
769 17. Abdelgawad AM, Watanabe K, Takeuchi S, Mizuno T. The origin of fluoride-rich
770 groundwater in Mizunami area, Japan—Mineralogy and geochemistry implications.
771 Engineering Geology. 2009; 108: 76–85. https://doi.org/10.1016/j.enggeo.2009.06.016.
772 18. Faure G. Principles and applications of inorganic geochemistry. Macmillan Publ. Co.,
773 New York, NY, 1991; pp. 626.
774 19. Edmunds WM, Smedley PL. Fluoride in natural waters. In: Selinus O (ed) Essentials of
775 medical geology. Elsevier Academic Press, London, 2005; pp 301–329.
776 20. Ayoob S, Gupta AK. Fluoride in drinking water: a review on the status and stress effects.
777 Critical Reviews in Environmental Science and Technology. 2006; 36: 433– 487.
778 https://doi.org/10.1080/10643380600678112.
779 21. Thakur B, Loganathan VA, Sharma A, Sharma RK, Parker A. Release of geogenic
780 fluoride from contaminated soils of Rajasthan, India: Experiments and geochemical

781 modeling. Water Security. 2023; 19: 100140.
782 https://doi.org/10.1016/j.wasec.2023.100140.
783 22. Haidouti C. Effects of fluoride pollution on the mobilization and leaching of aluminum
784 in soils. Science of the Total Environment. 1995; 166(1-3): 157-160.
785 https://doi.org/10.1016/0048-9697(95)04525-6.
786 23. Ghale Askari S, Oskoei V, Abedi F, Motahhari Far P, Naimabadi A, Javan S. Evaluation
787 of heavy metal concentrations in black tea and infusions in Neyshabur city and
788 estimating health risk to consumers. International Journal of Environmental Analytical
789 Chemistry. 2020; 102: 7928 – 7937. https://doi.org/10.1080/03067319.2020.1842388.
790 24. Gaciri SJ, Davies TC. The occurrence and geochemistry of fluoride in some natural
791 waters of Kenya. Journal of Hydrology. 1993; 143: 395–412.
792 https://doi.org/10.1016/0022-1694(93)90201-J.
793 25. Walna B, Kurzyca I, Siepak J. Variations in fluoride level in precipitation in a Region of
794 human impact. Water, Air, & Soil Pollution: Focus. 2007; 7: 33–40.
795 https://doi.org/10.1007/s11267-006-9108-4.
796 26. Feng YW, Ogura N, Feng ZW, Zhang F, Shimizu H. The concentrations and sources of
797 fluoride in atmospheric depositions in Beijing, China. Water, Air, & Soil Pollution. 2003;
798 145: 95–107. https://doi.org/10.1023/A:1023680112474.
799 27. Cronin SJ, Manoharan V, Hedley MJ, Loganathan P. Fluoride: a review of its fate,
800 bioavailability, and risks of fluorosis in grazed-pasture systems in New Zealand.
801 New Zealand Journal of Agricultural Research. 2000; 43: 295–321.
802 https://doi.org/10.1080/00288233.2000.9513430.
803 28. Guo Q, Wang Y, Ma T, Ma R. Geochemical processes controlling the elevated fluoride
804 concentrations in groundwaters of the Taiyuan Basin, Northern China. Journal of
805 Geochemical Exploration. 2007; 93: 1–12. https://doi.org/10.1016/j.gexplo.2006.07.001.
806 29. Kim K, Jeong GY. Factors influencing natural occurrence of fluoride-rich groundwaters:
807 a case study in the southeastern part of the Korean Peninsula. Chemosphere. 2005; 58:
808 1399–1408. https://doi.org/10.1016/j.chemosphere.2004.10.002.
809 30. Nogami K, Iguchi M, Ishihara K, Hirabayashi J, Miki D. Behavior of fluorine and
810 chlorine in volcanic ash of Sakurajima volcano, Japan in the sequence of its eruptive
811 activity. Earth, Planets and Space. 2006; 58: 595–600.
812 https://doi.org/10.1186/BF03351956
813 31. Farooqi A, Masuda H, Firdous N. Toxic fluoride and arsenic contaminated groundwater
814 in the Lahore and Kasur districts, Punjab, Pakistan and possible contaminant sources.

Environmental Pollution. 2007; 145: 839–849. https://doi.org/10.1016/j.envpol.2006.05.007.
32. Dharmagunawardhane HA, Disanayake CB. Fluoride problems in Sri Lanka. Environmental Management and Health.1993; 4: 9–16. https://doi.org/10.1108/09566169310033422.
33. Moghaddam AA, Fijani E. Distribution of fluoride in groundwater of Maku area, northwest of Iran. Environmental Geology. 2008; 56: 281–287. https://doi.org/10.1007/s00254-007-1163-2.
34. Asgari G, Salari M, Seidmohammadi A, Akbari-adergani B, Mahvi AH, Kamari N, Rastegar KE, Faraji H. Investigation and risk assessment of fluoride concentration in drinking water, soil and food products in Hamedan rural areas. Scientific Reports. 2025; 15: 18458. https://doi.org/10.1038/s41598-025-99462-2.
35. Haidouti C. Fluoride distribution in soils in the vicinity of a point emission source in Greece. Geoderma. 1991; 49: 129–138. https://doi.org/10.1016/0016-7061(91)90096-C.
36. Indermitte E, Saava A, Karro E. Exposure to high fluoride drinking water and risk of dental fluorosis in Estonia. International Journal of Environmental Research and Public Health. 2009; 6: 710–721. https://doi.org/10.3390/ijerph6020710.
37. Nanyaro JT, Aswathanarayana U, Mungure JS. A geochemical model for the abnormal fluoride concentrations in waters in parts of Northern Tanzania. Journal of African Earth Sciences. 1984; 2:129–140. https://doi.org/10.1016/S0731-7247(84)80007-5.
38. Cohen D, Conrad HM. 65,000 GPD fluoride removal membrane system in Lakeland, California, USA. Desalination. 1998; 117: 19–35. https://doi.org/10.1016/S0011-9164(98)00063-0.
39. Duraiswami RA, Patankar U. Occurrence of Fluoride in the Drinking Water Sources from Gad River Basin, Maharashtra. Journal of the Geological Society of India. 2011; 77 (2): 167–174. https://doi.org/10.1007/s12594-011-0020-9.
40. Patil S, Patil B, Kadam A, Wagh V, Patil A, Pimparkar A, Karuppannan S, Sahu U. Nitrate and fluoride contamination in the groundwater in a tribal region of north Maharashtra, India: An account of health risks and anthropogenic influence. Groundwater for Sustainable Development. 2024; 25: 101107. https://doi.org/10.1016/j.gsd.2024.101107.
41. Rao RNV, Rao N, Rao KSP, Schuiling RD. Fluorine distribution in waters of Nalgonda District, Andhra Pradesh, India. Environmental Geology. 1993; 21: 84–89. https://doi.org/10.1007/BF00775055.

42. Kumar S, Chauhan A, Kumar A, Kumar S, Gupta A, Roy S, Kumari SC. Dental fluorosis and associated risk factors in early adolescents in India. International Journal of Adolescent Medicine and Health. 2018; 32(4): 20170200. https://doi.org/10.1515/ijamh-2017-0200.
43. Yuan L, Fei W, Jia F, Jun-ping L, Qi L, Fang-ru N, Xu-dong L, Shu-lian X. Health risk in children to fluoride exposure in a typical endemic fluorosis area on loess plateau, North China, in the last decade. Chemosphere. 2020; 243: 125451. https://doi.org/10.1016/j.chemosphere.2019.125451.
44. Keramati H, Miri A, Baghaei M, Rahimizadeh A, Ghorbani R, Fakhri Y, Bay A, Moradi M, Bahmani Z, Ghaderpoori M, Khaneghah AM. Fluoride in Iranian drinking water resources: a systematic review, meta- analysis and non-carcinogenic risk assessment. Biological Trace Element Research. 2019; 188: 261–273. https://doi.org/10.1007/s12011-018-1418-7.
45. Karabulut YB, Derin P, Demir Yetiş A, Yeşilnacar MİR. Health risk assessment in an area of dental fluorosis disease from high fluoride drinking water: a case study from southeastern Türkiye. International Journal of Environmental Health Research. 2024; 34(5): 2299–2314. https://doi.org/10.1080/09603123.2023.2243848.
46. Swain T. Quantitative measurement of fluoride in acid-alkali leaching solution of fluoride contaminated soil, qualitatively in chemically treated soil and their thermal properties. Discover soil. 2025; 2: 32. https://doi.org/10.1007/s44378-025-00062-3.
47. Moon DH, Jo R, Koutsospyros A, Cheong KH, Park JH. Soil washing of fluorine contaminated soil using various washing solutions. Bulletin of Environmental Contamination and Toxicology. 2015; 94: 334–339. https://doi.org/10.1007/s00128-014-1449-5.
48. Murray F. Fluoride retention in highly leached disturbed soils. Environmental Pollution Series B: Chemical and Physical.1984; 7(2): 83-95. https://doi.org/10.1016/0143-148X(84)90010-7.
49. Weidong L, Baret F, Xingfa G, Qingxi T, Lanfen Z, Bing Z. Relating soil surface moisture to reflectance. Remote Sensing of Environment. 2002; 81: 238 – 246. https://doi.org/10.1016/S0034-4257(01)00347-9.
50. Neema DL, Shah A, Patel AN. A statistical optical model for light reflection and penetration through sand. International Journal of Remote Sensing. 1987; 8(8): 1209-1217. https://doi.org/10.1080/01431168708954765.

883 51. Mortimore JL, Marshall Lisa-J R, Almond MJ, Hollins P, Matthews W. Analysis of red
884 and yellow ochre samples from Clearwell Caves and Çatalhöyük by vibrational
885 spectroscopy and other techniques. Spectrochim. Spectrochimica Acta Part A: Molecular
886 and Biomolecular Spectroscopy. 2004; 60: 1179–1188.
887 https://doi.org/10.1016/j.saa.2003.08.002.
888 52. Moss TS. Relations between the Refractive Index and Energy Gap of Semiconductors.
889 Physica status solidi. B, Basic research. 1985; 131(2): 415-427.
890 https://doi.org/10.1002/pssb.2221310202.
891 53. Herve P, Vandamme LKJ. General relation between refractive index and energy gap in
892 semiconductors. Infrared Physics and Technology.1994; 35(4): 609-615.
893 https://doi.org/10.1016/1350-4495(94)90026-4.
894 54. Tiruneh GA, Meshesha DT, Adgo E, Tsunekawa A, Haregeweyn N, Fenta AA, Belay
895 AW, Tadesse N, Fekadu G, Reichert JM. Use of soil spectral reflectance to estimate
896 texture and fertility affected by land management practices in Ethiopian tropical
897 highland. PLoS ONE 2022; 17(7): e0270629.
898 https://doi.org/10.1371/journal.pone.0270629.
899 55. Chiromawa IM, Shaari A, Razali R, Ahams ST, Abdullahi M. Ab initio Investigation
900 of the Structure and Electronic Properties of Normal Spinel Fe_2SiO_4. Malaysian Journal
901 of Fundamental and Applied Sciences. 2021; 17(2): 195-201.
902 https://doi.org/10.11113/mjfas.v17n2.2018.
903 56. Montoya-Bautista CV, Acevedo-Peña P, Zanella R, Ramírez-Zamor Rosa-M.
904 Characterization and Evaluation of Copper Slag as a Bifunctional Photocatalyst for
905 Alcohols Degradation and Hydrogen Production. Topics in Catalysis. 2021; 64: 131–141.
906 https://doi.org/10.1007/s11244-020-01362-4.
907 57. Bernsmeier D, Polte J, Ortel E, Krahl T, Kemnitz E, Kraehnert R. Antireflective
908 Coatings with Adjustable Refractive Index and Porosity Synthesized by Micelle-
909 Templated Deposition of MgF_2 Sol Particles. ACS Applied Materials & Interfaces. 2014;
910 6(22): 19559–19565. https://doi.org/10.1021/am5052685.
911 58. DuMont JW, George SM. Competition Between Al_2O_3 Atomic Layer Etching and AlF_3
912 Atomic Layer Deposition Using Sequential Exposures of Trimethylaluminum and
913 Hydrogen Fluoride. Journal of Chemical Physics. 2017; 146: 052819.
914 https://doi.org/10.1063/1.4973310.
915 59. Sundaram CS, Viswanathan N, Meenakshi S. Defluoridation chemistry of synthetic

hydroxyapatite at nano scale: equilibrium and kinetic studies. Journal of Hazardous Materials. 2008; 155(1-2): 206-215. https://doi.org/10.1016/j.jhazmat.2007.11.048.

60. Stein M, Georgiadis A, Gudat D, Rennert T. Formation and properties of inorganic Si-contaminant compounds. Environmental Pollution. 2020; 265: 115032. https://doi.org/10.1016/j.envpol.2020.115032.
61. Bishop JL, Rampe EB, Bish DL, Abidin Z, Baker LL, Matsue N, Henmi T. Spectral and hydration properties of allophane and imogolite. Clay Minerals. 2013; 61: 57–74. https://doi.org/10.1346/CCMN.2013.0610105.
62. Andrews L, Lascola R. Infrared spectra of the ammonia-fluorine and fluoramide-hydrogen fluoride complexes in solid argon. Journal of the American Chemical Society. 1987; 109(21): 6243–6247. https://doi.org/10.1021/ja00255a004.
63. Eksperiandova LP, Fedorov AI, Stepanenko NA, Blank TA. Method for Water Determination Using an Elemental Analyzer. Inorganic Materials. 2011; 47(15): 1635–1639. https://doi.org/10.1134/S0020168511150052.
64. Wang Y, Lu S, Ren T, Li B. Bound water content of air-dry soils measured by thermal analysis. Soil Science Society of America Journal. 2011; 75(2): 481-487. https://doi.org/10.2136/sssaj2010.0065.
65. Balek V, Subrt J. Thermal behaviour of iron(111) oxide hydroxides, Pure and Applied Chemistry. 1995; 67(11): 1839-1842. https://doi.org/10.1351/pac199567111839.
66. Yang GY, Shi YCh, Liu XD, Mujumdar AS. TG-DTG Analysis of Chemically Bound Moisture Removal of $AlF_3 \cdot 3H_2O$. Drying Technology. 2007; 25: 675– 680. https://doi.org/10.1080/07373930701285993.
67. Rodriguez ET, Garbev K, Merz D, Black L, Richardson IG. Thermal stability of C-S-H phases and applicability of Richardson and Groves' and Richardson C-(A)-S-H(I) models to synthetic C-S-H. Cement and Concrete Research. 2017; 93: 45–56. https://dx.doi.org/10.1016/j.cemconres.2016.12.005.
68. Siewert C. Rapid Screening of Soil Properties using Thermogravimetry. Soil Science Society of America Journal. 2004; 68(5): 1656–1661. https://doi.org/10.2136/sssaj2004.1656.
69. Tokarski D, Kučerík J, Kalbitz K, Demyan MS, Merbach I, Barkusky D, Ruehlmann J, Siewert C. Contribution of organic amendments to soil organic matter detected by thermogravimetry. Journal of Plant Nutrition and Soil Science. 2018; 181(5): 664-674. https://doi.org/10.1002/jpln.201700537.

70. Pribyl DW. A critical review of the conventional SOC to SOM conversion factor. Geoderma. 2010; 156(3-4), 75-83. https://doi.org/10.1016/j.geoderma.2010.02.003.
71. Arunrat N, Kongsurakan P, Sereenonchai S, Hatano R. Soil Organic Carbon in Sandy Paddy Fields of Northeast Thailand: A Review. Agron. 2020; 10(8): 1061. https://doi.org/10.3390/agronomy10081061.
72. Gangadhara Rao MVBB, Kolay PK, Singh DN. Thermal characteristics of a class F fly ash. Cement and Concrete Research. 1998; 28(6): 841-846. https://doi.org/10.1016/S0008-8846(98)00054-4.
73. Abu-Hamdeh NH. Thermal Properties of Soils as affected by Density and Water Content. Biosystems Engineering. 2003; 86 (1): 97–102. https://doi.org/10.1016/S1537-5110(03)00112-0.
74. Wang Y, Lu Y, Horton R, Ren T. Specific Heat Capacity of Soil Solids: Influences of Clay Content, Organic Matter, and Tightly Bound Water. Soil Science Society of America Journal. 2019; 83(4):1062-1066. https://doi.org/10.2136/sssaj2018.11.0434.
75. Sur SK, Bryant RG. ^{19}F and ^{27}AI n.m.r. spectroscopic study of the fluoro complexes of aluminum in aqueous solution and zeolites: Dealumination of zeolites by fluoride ions. Zeolites. 1996; 16(2-3): 118-124. https://doi.org/10.1016/0144-2449(95)00108-5.
76. Nguyen TQ, Qu F, Huang X, Janzen AF. Preparation and NMR spectra of $PF_4(N\text{-}N)^+$ and $SiF_4(N\text{-}N)$, where N-N = 2,2′-bipyridine, 4-fluoro-2,2′-bipyridine, and 1,10-phenanthroline. Canadian Journal of Chemistry. 1992;70(7): 2089-2093. https://doi.org/10.1139/v92-265
77. Fischer L, Harle V, Kasztelan S, d'Espinose de la Caillerie J-B. Identification of fluorine sites at the surface of fluorinated γ-alumina by two-dimensional MAS NMR. Solid State Nuclear Magnetic Resonance. 2000; 16: 85–91. https://doi.org/10.1016/S0926-2040(00)00058-8.
78. Sun Ming-H, Gao Shu-S, Hu Zhi-Y, Barakat T, Liu Z, Yu S, Lyu Jia-M, Li Y, Xu Shu-T, Chen Li-H, Su Bao-L. Boosting molecular diffusion following the generalized Murray's Law by constructing hierarchical zeolites for maximized catalytic activity. National Science Review. 2022; 9(12): nwac236. https://doi.org/10.1093/nsr/nwac236.
79. Boxhoorn G, Kortbeek AGTG, Hays GR, Alma NCM. A high-resolution solid-state ^{29}Si n.m.r. study of ZSM-5 type zeolites. Zeolites. 1984; 4(1): 15–21. https://doi.org/10.1016/0144-2449(84)90066-6.
80. Wang W, Xu J, Deng F. Recent advances in solid-state NMR of zeolite catalysts. National Science Review. 2022; 9(9): nwac155. https://doi.org/10.1093/nsr/nwac155.

81. Hiradate S. Speciation of Aluminum in Soil Environments Application of NMR Technique. Journal of Soil Science and Plant Nutrition. 2004; 50(3): 303-314. https://doi.org/10.1080/00380768.2004.10408483.
82. Chen K, Gan Z, Horstmeier S, White JL. Distribution of Aluminum Species in Zeolite Catalysts: ^{27}Al NMR of Framework, Partially-Coordinated Framework, and Non-Framework Moieties. Journal of the American Chemical Society. 2021; 143(17): 6669−6680. https://doi.org/10.1021/jacs.1c02361.
83. Losch P, Pinar AB, Willinger MG, Soukup K, Chavan S, Vincent B, Pale P, Louis BH. ZSM-5 zeolite model crystals: Structure-diffusion-activity relationship in methanol-to-olefins catalysis. Journal of Catalysis. 2017; 345: 11-23. https://doi.org/10.1016/j.jcat.2016.11.005.
84. Bra¨uniger T, Kempgens P, Harris RK, Howes AP, Liddell K, Thompson DP. A combined ^{14}N/^{27}Al nuclear magnetic resonance and powder X-ray diffraction study of impurity phases in β-sialon ceramics. Solid State Nuclear Magnetic Resonance. 2003; 23(1-2): 62–76. https://doi.org/10.1016/S0926-2040(02)00016-4.
85. Müller D, Gessner W, Samoson A, Lippmaa E, Scheler G. Solid-state ^{27}Al NMR studies on polycrystalline aluminates of the system CaO-Al_2O_3. Polyhedron 1986; 5(3): 779-785. https://doi.org/10.1016/S0277-5387(00)84437-X.
86. Kobera L, Dedecek J, Klein P, Tabor E, Brus J, Fishchuk AV, Sklenak S. Formation and local structure of framework Al Lewis sites in beta zeolites. Journal of Chemical Physics. 2022; 156:104702. https://doi.org/10.1063/5.0083666.
87. Jiao J, Kanellopoulos J, Wang W, Ray SS, Foerster H, Freude D, Hunger M. Characterisation of framework and extra-framework aluminium species in non-hydrated zeolites Y by 27Al spin-echo, high-speed MAS, and MQMAS NMR spectroscopy at B_0= 9.4 to 17.6 T. Physical Chemistry Chemical Physics. 2005; 7(17): 3221–3226. https://doi.org/10.1039/B508358C.
88. Kao Hsien-M, Chen Yun-C. ^{27}Al and ^{19}F Solid-State NMR Studies of Zeolite H-β Dealuminated with Ammonium Hexafluorosilicate. Journal of Physical Chemistry B. 2003; 107: 3367-3375. https://doi.org/10.1021/jp021680q.
89. Garcia-Lodeiro I, Palomo A, Fernández-Jiménez A, Macphee DE. Compatibility studies between N-A-S-H and C-A-S-H gels. Study in the ternary diagram Na_2O–CaO–Al_2O_3–SiO_2–H_2O. Cement and Concrete Research. 2011; 41(9): 923-931. https://doi.org/10.1016/j.cemconres.2011.05.006.

90. Mausbach K, Nowack N, Schlegelmilch F. Structural statements, coordination numbers and water vapour solubility in aluminate slags. Steel Research International. 1993; 64(5): 239- 245. https://doi.org/10.1002/srin.199301016.
91. Hoyos-Montilla AA, Puertas F, Mosquera JM, Tobón JI. Infrared spectra experimental analyses on alkali-activated fly ash-based binders. Spectrochimica Acta Part A: Molecular and Biomolecular Spectroscopy. 2022; 269: 120698. https://doi.org/10.1016/j.saa.2021.120698.
92. Kucharık M, Korenko M, Janickovic D, Kadlecıkova M, Boca M, Obona JV. Rapid solidification of cryolite and cryolite–alumina melts. Monatshefte für Chemie. 2010; 141: 7–13. https://doi.org/10.1007/s00706-009-0229-0.
93. Goebbert DJ, Garand E, Wende T, Bergmann R, Meijer G, Asmis KR, Neumark, DM. Infrared Spectroscopy of the Microhydrated Nitrate Ions $NO_3^-(H_2O)_{1-6}$. Journal of Physical Chemistry A. 2009; 113(26): 7584–7592. https://doi.org/10.1021/jp9017103.

Supplementary Files

This is a list of supplementary files associated with this preprint. Click to download.

- SupplementaryFigures.docx
- GraphicalAbstract.jpg